

Andrea Gmür

Design of a Dual-phase Xenon Time-projection Chamber with a Hybrid Photosensor Arrays

Master Thesis

Physik-Institut
University of Zurich

Supervision

Prof. Dr. Laura Baudis
Dr. Alexander Kish

Contents

Abstract	iii
Nomenclature	v
1 Dark Matter	1
1.1 Cosmological Observations	1
1.1.1 Galactic Observations	1
1.1.2 Gravitational Lensing	3
1.2 Dark Matter Candidates	3
1.3 Dark Matter Detection	5
1.3.1 Direct Detection	5
2 Time-Projection Chamber for Dark Matter Detection	9
2.1 Time-Projection Chamber	9
2.1.1 Double Phase TPC	9
2.1.2 Noble Gas as Target Material	10
2.1.3 Background Sources and Reduction Techniques	11
2.2 XENON Experiments	13
2.2.1 DARWIN	14
2.3 Overview of the MarmotXL TPC Project	16
2.3.1 TPC for MarmotXL	16
2.3.2 MarmotXL	16
2.3.3 Photodetectors	17
2.3.4 Design and Simulation	17
3 Photomultiplier Tube	19
3.1 General Description	19
3.1.1 Quantum Efficiency	20
3.1.2 Dark Counts	20
3.1.3 Afterpulse	20
3.1.4 Gain (Current Amplification)	21
3.2 Model R8520-406	21
3.3 Gain Measurements	22
3.3.1 General Set-up Requirements	22
3.3.2 Electronic Equipment	23
3.3.3 Data Acquisition and Processing	23
3.3.4 Gain Measurement	25
3.4 Measurements Time Line	26
3.4.1 Black Box	26
3.4.2 SandBox	26
3.5 Results and Conclusions	28
3.5.1 Gain HV Dependency	28
3.5.2 Resolution	29

3.5.3	Conclusions and Outlook	30
4	Semiconductor Photosensors	31
4.1	General Description	31
4.1.1	From Semiconductors to Diodes	31
4.1.2	Avalanche Photodiodes	32
4.1.3	Multi-Pixel Photon Counter	33
4.1.4	3x3 mm ² MPPC Models	35
4.2	Experimental Set-up	35
4.2.1	General Set-up Requirements	35
4.2.2	Liquid Argon Set-up	36
4.2.3	Electronic Equipment	37
4.3	MPPC Gain Measurement	38
4.3.1	Gain Calculation	38
4.3.2	First Test in MarmotXL	39
4.3.3	Black Box	39
4.3.4	LArS	40
4.4	Results and conclusions	41
4.4.1	Gain at Room Temperature	41
4.4.2	Conclusions and Outlook	41
5	Design and Monte Carlo simulation of a Time-Projection Chamber	43
5.1	Monte Carlo Simulations	43
5.1.1	TPC Geometry	43
5.1.2	Material Properties	44
5.1.3	Software Support	44
5.1.4	Simulation Parameter	44
5.1.5	Bottom and Top Arrays	44
5.1.6	Code Evolution	46
5.1.7	Analysis of S2 Simulations	46
5.1.8	Analysis of S1 Simulations	50
5.2	Technical Drawing	52
5.2.1	Design of the Top Photodetector Array Holder	52
5.3	Conclusion to the TPC Project	54
6	Summary	57
7	Acknowledgement	59

Abstract

The goal of this thesis was to design a dual-phase Time-Projection Chamber (TPC), based on MPPC and ADP read-out, using xenon in liquid and gas phase. This detector type is in use for dark matter searches a component of the universe that escaped direct detection until now. The TPC discussed in this thesis has a target of 7.8 kg of liquid xenon and will include 3-inch and 1-inch photomultiplier tubes and silicon photosensors, such as avalanche photodiode and multi-pixel photon counter (MPPC). This project aims to test the reliability of MPPC for dark matter experiments, since their detection surface relative to their mass is much higher than that of conventionally used photomultiplier tubes. This would reduce the background arising from radioactivity of material, allowing the dark matter investigation to lower cross-sections. Once in operation, the TPC can also be used for studies aiming to improve the position reconstruction at high energy. This work is divided into three parts;

Vacuum Photomultiplier Tube (TPC) characterisation; in order to be able to operate all the PMTs at the same gain, studies of the gain dependency with respect to the high voltage must be performed. An LED was used as a controlled light source, and the signal was triggered by the LED pulse generator. The gain has been characterized for 23 1-inch PMTs.

Multi-Pixel Photon Counter (MPPC) characterisation; a new set-up capable to read out the signal of this sensor type has been realised to conduct the necessary studies for constructing a xenon-based TPC with Si-photosensors readout. The gain measurements were performed at room temperature and pressure. Furthermore, some results obtained at lower temperatures are presented. The gain dependency on the temperature and supply voltage have been characterized.

Design and simulations of the TPC were performed using Geant4 and SolidWorks. The goal of the simulations was to define the best configuration for the top photodetector array and to provide information about the light collection efficiency of the S1 and S2 signals. Once the geometry was defined, the technical drawing for the realization of the PTFE top array holder had to be done. This had to take into account such factors as the PTFE thermal contraction at low temperatures and the mechanical precision provided by the workshop machine.

Nomenclature

Acronyms and Abbreviations

APD	Avalanche Photodiode
BB	Black Box
BSM	Beyond the Standard Model
CDM	Cold Dark Matter
SCS	Slow Control System
DC	Dark Current
DDS	Direct Digital Synthesis
DM	Dark Matter
FADC	Flash Analog-to-Digital Converter
GXe	Gaseous Xenon
HV	High Voltage
LCE	Light Collection Efficiency
LED	Light Emitting Diode
LArS	Liquid Argon Set-up
LNGS	Laboratori Nazionali del Gran Sasso
LXe	Liquid Xenon
MPPC	Multi-Pixel Photon Counter
PS	Photodetector
PE	Photoelectron
PMT	Photomultiplier Tube
PQ	Peccei and Quinn
PTFE	Polytetrafluoroethylene
PTR	Pulse Tube Refrigerator
SHM	Standard Halo Model
SPE	Single Photoelectron
TPC	Time-Projection Chamber
QCD	Quantum Chromodynamics
WIMP	Weakly Interacting Massive Particle

Chapter 1

Dark Matter

The nature of the composition of the universe is mostly unknown. In the past century, cosmological observations suggested that only 4.9% of the universe's total energy density consists of visible matter that is traditionally observed. The rest of the content is made up of dark matter (DM) and dark energy. The first of these refers to matter that interacts only weakly or gravitationally with normal matter, while the second, which is far less known, is responsible for the present day acceleration of the universe expansion [1].

In the Standard Model of Big Bang Cosmology (Λ CDM - cosmological constant and cold dark matter [2]), the dark matter is understood to be a non-relativistic weakly interacting particle or sets of particles responsible for the accelerated transition of the universe from radiation-dominated to matter-dominated [3]. Λ CDM in conjunction with cosmological observations has demonstrated that dark matter, as opposed to luminous baryonic matter, makes up over 80% of the total matter content of the universe and roughly 25.9% of its total energy density [4]. The largest component, 69.1% of the energy density, is made up by dark energy.

1.1 Cosmological Observations

The first hints of the existence of dark matter came relatively early in the history of extragalactic astronomy. In the 1930s, Fritz Zwicky noticed that the outlying galaxies in the Coma galaxy cluster are moving around the cluster centre much faster than expected, based on the amount of luminous matter present [5]. More than 70 years of observation later, from small scale galaxies to cosmic microwave radiation, the composition of this matter is still unknown.

1.1.1 Galactic Observations

The first observation suggesting the existence of dark matter in galaxies was obtained measuring the rotation velocity curves of stars in spiral galaxy [6]. These observations showed that spiral galaxies have flat rotation curves extending out to radii of tens of kpc (1 kpc $\sim 3 \cdot 10^{19}$ m). The discrepancy between the velocity expected from the luminous disk compared to the one observed led to the conclusion that galaxies must have considerable mass beyond the optically-visible matter (figure 1.1). From Newton's law of gravitation, galactic velocities are expected to follow:

$$v(r) = \sqrt{\frac{G_N M(r)}{r}}, \quad (1.1)$$

where $M(r) = 4\pi \int \rho(r)r^2 dr$ denotes the mass distribution with the radial dependent density $\rho(r)$. Considering the observable mass distribution of the disk, the velocity is supposed to fall such that $v(r) \propto 1/\sqrt{r}$ is beyond its bounds. However, the observation of a flat curve requires $\rho(r) \propto 1/r^2$ in order to have a constant velocity. Under the assumption of collisionless gas, weakly interacting dark matter with isotropic initial velocity distribution its equation of state is given by

$$p(r) = \rho(r) \cdot \sigma^2, \quad (1.2)$$

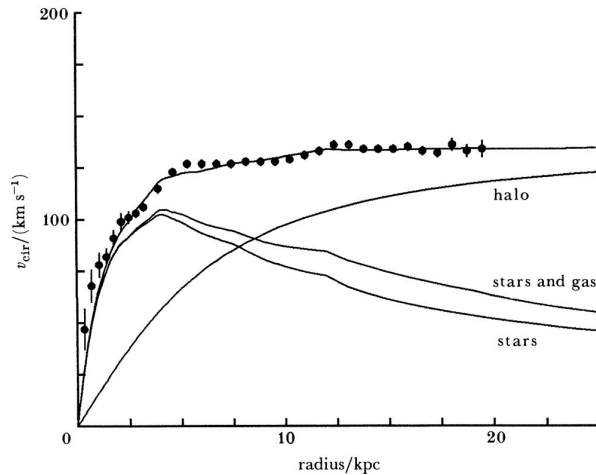


Figure 1.1: The rotation curve of spiral galaxy NGC 2403, shows the actual velocities of its outer stars (plotted points). The velocities expected from the visible mass distribution and also considering the gas component are represented. The data are fitted overlaying the second curve to the assumed contribution of the mass of a dark matter halo. Figure from [7].

where the pressure is given by the density ρ and the velocity dispersion σ . Imposing the system to be in a hydrostatic equilibrium the pressure is balancing the gravity:

$$\frac{dp(r)}{dr} = -G \frac{M(r)}{r^2} \rho(r). \quad (1.3)$$

The expressions given in equations 1.2 and 1.3 can be rearranged as follows:

$$\frac{r^2}{\rho(r)} \frac{d\rho(r)}{dr} = -\frac{1}{\sigma^2} GM(r). \quad (1.4)$$

After differentiating this expression and using the equation of conservation of mass ($\frac{dM}{dr} = 4\pi r^2 \rho(r)$) the density distribution $\rho(r)$ is found to be

$$\rho(r) = \frac{\sigma^2}{2\pi G r^2}, \quad (1.5)$$

corresponding to a spherical configuration. This is the reason why it is called *the dark matter halo*. Considering the density distribution of a spherical dark matter halo to be an isothermal sphere [8]:

$$\rho_{halo}(r) = \rho_0 \left[1 + \frac{r}{r_c} \right], \quad (1.6)$$

where r_c is the radius of the halo core and ρ_0 is the DM density at the solar radius R_0 . The Standard Halo Model (SHM) assumes a specific value of local dark matter density and specifies the velocity to follow a Maxwell-Boltzmann distribution for collisionless particle with a cut-off at the escape velocity. The parameters are [9]:

- local density $\rho_0 = \rho(R_0) = 0.3 \text{ GeV cm}^{-3}$
- local circular speed $v_c = 220 \text{ km s}^{-1}$
- local escape speed $v_{esc} = 533 \text{ km s}^{-1}$

1.1.2 Gravitational Lensing

A gravitational lens refers to a distribution of matter (such as a cluster of galaxies) between a distant source and an observer, that is capable of bending the light from the source, as it travels towards the observer. This effect is known as gravitational lensing and is one of the predictions of Albert Einstein's General Theory of Relativity [10]. The gravitational lensing effect can be classified in three groups depending of the deflection power: strong, weak and micro-lensing. Strong gravitational lensing happens when there is so much mass contrast in the lens that the light rays from a distant source form multiple images. This was first seen in a quasar lensed by a galaxy in 1979 (figure 1.2)[11].

In weak lensing effect the distortions of background sources are much smaller and can only be detected by analysing large numbers of sources to find coherent distortions of only a few percent. The lensing shows up statistically as a preferred stretching of the background objects perpendicular to the direction to the center of the lens. By measuring the shapes and orientations of large numbers of distant galaxies, their orientations can be averaged to measure the shear of the lensing field in any region. This, in turn, can be used to reconstruct the mass distribution in the area: in particular, the distribution of dark matter can be reconstructed [12]. Microlensing presents no distortion in shape, but the amount of light received from a background object changes in time, when passing behind the lens.

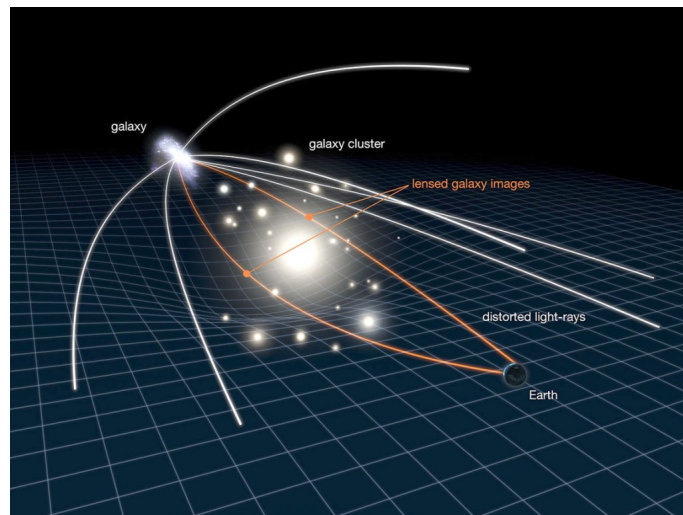


Figure 1.2: The light rays from the distant galaxy are bent when passing a large gathering of mass. When the light arrives at the Earth, it is observed as coming from a slightly different direction. From the bending of the light, the mass of the galaxy cluster can be calculated. Computing the difference between this mass and the visible mass, the amount of DM can be extrapolated. Figure from [11].

1.2 Dark Matter Candidates

An increasing number of astrophysical and astronomical observations point to the existence of a cold (i.e. non-relativistic) dark matter component in the universe, hence called Cold Dark Matter (CDM) [13].

In briefly reviewing the history of the universe, it is evident that stable particles in the early universe (possibly dark matter) could have a considerable cosmological abundance today [14]. The early universe was in thermal equilibrium, maintained through an equivalent annihilation and production rate of all particles. The expansion and cool down of the universe could have caused these stable particles to fall out of thermal equilibrium leaving behind a relic cosmological abundance that can

be attributed to dark matter. In order to describe this leftover density several theories Beyond the Standard Model (BSM) have been introduced, which contain possible dark matter candidates. The most studied candidates are the Weakly Interacting Massive Particles (WIMPs), including the supersymmetric neutralinos, followed by axions.

WIMPs

This type of DM candidate has been introduced by Steigman and Turner (1985) [15] and represents a general class of dark matter candidates that may be thermal relics of the Big Bang. In the early universe, when it was very hot and dense, all particle species were in thermal and chemical equilibrium. The hot and dense universe cooled down through the expansion, and at the point the temperature was below the WIMP mass, m_χ , the co-moving density (the density ignoring the expansion of space) of WIMPs decreased exponentially with its temperature according to the Boltzmann factor $e^{(m_\chi/T)}$ as a result of self-annihilation. This density dropping process is then suppressed by the further universe expansion. When the self-annihilation rate becomes smaller than the Hubble expansion rate, WIMPs *freeze-out*, meaning that they chemically decouple from the thermal equilibrium. Through continuous universe expansion the WIMPs co-moving density approached a constant. The resulting relic number density of χ -particles then depends only on the ratio of the annihilation cross-section of χ and the Hubble scale near the freeze-out temperature. For WIMPs this ratio agrees with that deduced from astrophysical and cosmological experiments [16]. This match is referred to as the *WIMPs miracle*. The relic density does not provide direct information concerning the WIMP mass, but on dimensional grounds [17] and under the weak coupling assumption, it can postulate to be in the range of $30 \text{ GeV}/c^2 - 1 \text{ TeV}/c^2$, which coincides with the weak scale. The fact that a weak scale particle is interacting through the weak force in addition to the WIMPs miracle is a motivation to consider WIMPs as excellent dark matter candidates.

Theoretical framework BSM like the *supersymmetry models* or extra spatial dimensions have been developed in order to address the gauge hierarchy problem. These theories, that require new particle at the weak scale, could be powerfully validated through the discovery of the WIMP. This is the major reason why the WIMPs are the widely most studied dark matter candidate. Supersymmetric neutralino (the lowest-mass eigenstate of the supersymmetric partners of neutral Standard Model gauge bosons) is a candidate in the WIMP class. It emerges out of supersymmetry theory SUSY (Jungman et al., 1996) that introduces new physics at the electroweak breaking scale [2]. WIMPs attributed properties offer numerous possibilities to detect them with existing or coming in the near future technologies. This is a further reason that justifies WIMPs' prominence. Since WIMPs must annihilate to other particles to yield the observed relic density, in conventional particle physics framework they can produce three types of observable signatures produced by annihilation (early universe), production and scattering as shown in figure 1.3.

Axion

The axion was proposed as a natural new light pseudo-scalar boson resulting from the solution to the charge-parity (CP) conservation problem of the strong interactions [18]. In quantum chromodynamics (QCD) theory the CP is violated, but experimentally this violation has never been observed. The problem was solved by introducing a field component in the QCD Lagrangian that can be spontaneously broken (PQ-symmetry). Breaking this symmetry, a pseudo-Goldstone boson is obtained, this is the axion. As shown in eq. 1.7 the mass m_a of the obtained axion is proportional to one over the scale factor of the broken PQ-symmetry f_a :

$$m_a \propto \frac{1}{f_a}. \quad (1.7)$$

Neither of these parameters is known, so the mass constraints for the axion are given by observations and experiments. Only the two mass windows $10^{-6} - 10^{-3} \text{ eV}/c^2$ and $2 - 5 \text{ eV}/c^2$ have to be investigated. The region between $2.3 \mu\text{eV}$ and $3.4 \mu\text{eV}$ has been investigated using the Sikivie radio frequency cavity technique, but no signal was detected [19].

1.3 Dark Matter Detection

The dark matter detection techniques can be divided in three groups as schematized in figure 1.3. An exhaustive discussion on the direct detection methods is given in section 1.3.1 and an overview of the two other methods follows below.

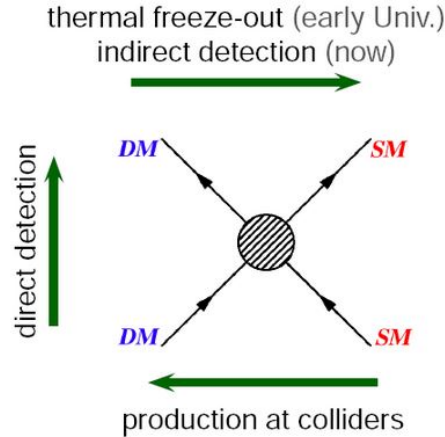


Figure 1.3: Interaction of dark matter with Standard Model particles. Based on the type of interaction three different approaches are used: indirect detection, direct detection, and production in collider experiments. Figure from [20].

Indirect detection: Indirect searches for DM aim at detecting the signatures of the annihilations or decays of DM particles in the flux of cosmic rays in a broad sense. These include: charged particles (electron and positron, proton and anti-proton, deuterium and anti-deuterium), photons, neutrons. Pioneering works have explored this as a promising way for new discovery since the late-70's. In general, a key point of all these searches is to look for channels and ranges of energy where it is possible to transcend the background from ordinary astrophysical processes [21].

Direct production: For some of the existing theories the postulated dark matter mass is small enough to be produced at a collider such as the Large Hadron Collider [22]. If dark matter particles were created during the collision, they would escape through the detectors unnoticed. However, they would carry away energy and momentum, so their existence could be inferred from the amount of energy and momentum 'missing' after a collision. The difficulty lies in the fact that, in order to know what is missing, all the other produced particles have to be recognized. Neutrinos can easily escape detection and be misidentified as dark matter, thus they represent a significant background.

1.3.1 Direct Detection

The incentive for direct WIMPs detection experiments derives from the fact that, if they exist, they may interact with baryonic matter weakly and become detected with technologies that are already in existence or being currently developed. WIMPs with masses of $(10-1000) \text{ GeV}/c^2$ would elastically scatter off nuclei in the target material and produce nuclear recoils in the range of $(1-100) \text{ keV}$ [23].

Direct WIMP Search Method

The theoretical basis for WIMP nuclear recoil detection is outlined extensively by Jungman, Kamionkowski, and Griest [24], and Lewin and Smith [25]. The Earth is moving through the DM halo with a mean velocity $v_0 \sim 220 \text{ km/s}$ (figure 1.4). In this way it is possible that a WIMP

transfers part of its kinetic energy to atomic matter during collisions. This is called recoil energy E_R and, as given in equation 1.8, is proportional to the WIMP energy (E_χ), the kinematic factor r and the WIMP scattering angle θ (see figure 1.5). The kinematic factor r is related to the reduced collision mass μ by $4\mu^2 = m_\chi m_T r$, where m_χ and m_T refer to the WIMP and target mass, respectively.

$$E_R = E_\chi r \frac{1 - \cos \theta}{2} \quad (1.8)$$

Since the energy transferred is of the order of a few keV and the nuclear energy levels are at MeV scales, the collisions are usually taken as elastic.

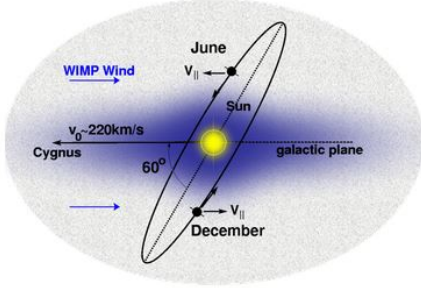


Figure 1.4: Illustration of the velocity components behind the annual modulation in a WIMP signal. Figure from [26].

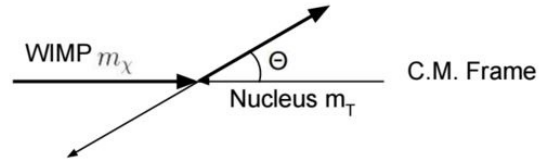


Figure 1.5: An illustrative WIMP interaction with matter in the centre of momentum frame.

$E_\chi = m_\chi v^2/2$ corresponds to the kinetic energy of the WIMP. It is evident from equation 1.8 that the maximum recoil energy is obtained for $\theta = \pi$ and corresponds to:

$$E_R \leq E_\chi r = \frac{1}{2} m_T v^2 \left(\frac{2m_\chi}{m_\chi + m_T} \right)^2. \quad (1.9)$$

Assuming a Maxwell-Boltzmann velocity distribution with respect to the galactic frame for the WIMP velocity $f(v)$, the relative motion of the Sun, the WIMPs scattering off nuclei, which have a finite size, then the detection rate can be written as:

$$R = \int_{E_T}^{\text{inf}} dE_R \frac{\rho_0}{m_n m_\chi} \int_{v_{\min}}^{\text{inf}} v f(v) \frac{d\sigma_{WN}}{dE_R}(v, E_R) dv, \quad (1.10)$$

where the energy threshold E_T and the minimal velocity v_{\min} are correlated to the detector efficiency. The detection rate decreases for heavier dark matter particles given the reduction of particles available for scattering, since the local dark matter density is a constant. WIMP-nucleon cross-section can be separated into a spin-independent (scalar) and a spin-dependent (axial-vector) contribution:

$$\frac{d\sigma_{WN}}{dE_R} = \left(\frac{d\sigma_{WN}}{dE_R} \right)_{SI} + \left(\frac{d\sigma_{WN}}{dE_R} \right)_{SD}. \quad (1.11)$$

Spin-independent interaction: During a WIMP-nucleus collision, the WIMP may interact with any of the A nucleons of the target nucleus:

$$\sigma_{SI} = \frac{m_N^2}{4\pi(m_\chi + m_N)^2} \cdot [Zf_p + (A - Z)f_n]^2, \quad (1.12)$$

where f_i is effective coupling to protons and neutrons, Z the atomic number and A the mass number. Assuming $f_n = f_p$ the cross-section $\sigma_{SI} \propto (Af_{n,p})^2$. In such a form, it is clear that for

the spin-independent WIMPs interactions, the cross-section increases with the mass of the target nucleus.

Spin-dependent interaction: Besides spin-independent interactions, WIMP and nuclei could also undergo axial vector ones in which WIMPs couple to the spin of the nucleus. In this case, the sum of the scattering amplitudes from individual nucleons gets complicated by the spin distribution inside a nucleus. The simplest model assumes that the scattering amplitudes from nucleons with opposite spin states cancel, and only unpaired nucleons contribute to the total cross-section:

$$\sigma_{SD} \propto \frac{J_N + 1}{J_N}, \quad (1.13)$$

where J_N represents the unpaired nuclear spin.

WIMP Direct Detection Experiments

Equation 1.10 provides the interaction rate of WIMPs with the target material of an experiment. The current sensitivity of direct dark matter search almost reached 10^{-46} cm^2 for the mass region around $50 \text{ GeV}/c^2$. No dark matter particles have been observed yet. With a hypothetical WIMP-nucleon interaction cross-section of 10^{-45} cm^2 at a WIMP mass of $100 \text{ GeV}/c^2$ and using the SHM parameters, and the velocity of the solar system $v_\odot = 220 \text{ km/s}$ around the galactic centre, the expected rate can be calculated. The attempt to measure the recoil energy dependence of dark matter interactions is the most common approach in direct detection experiments. The recoil energy is commonly expressed in nuclear recoil equivalent energy (keV_{nr} or keV_r) or in electron equivalent energy (keV_{ee}). The reason for this distinction is due to the difference in light quenching in the detector target between the two types of interactions. For example, the quenching factor for nuclear recoils in a liquid target scintillator is the ratio of the amount of light induced by a recoil nucleus to the amount of light induced by an electron of the same kinetic energy. The resulting rates for different target masses and WIMPs masses are represented in figure 1.6.

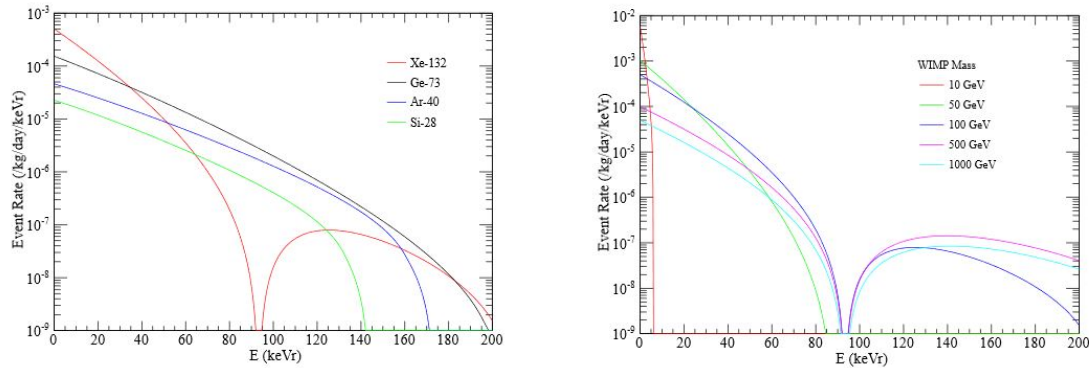


Figure 1.6: Left: the expected nuclear recoil spectra induced by $100 \text{ GeV}/c^2$ WIMPs through spin-independent interactions with different target materials. Right: Expected WIMP rate ($/\text{kg}/\text{day}/\text{keV}_r$) as a function of the deposited energy for different WIMPs masses for a xenon target. Cross-section is assumed to be 10^{-45} cm^2 in both plots. Figure from [1].

Two further dark matter signatures are the so-called *annual modulation* and the *directionality*. Both of them arise as a consequence of the Earth motion around the Sun and for the second also the Earth rotation itself. The annual modulation signature is a variation of the total event rate as a consequence of the changes in speed with which the experiment travels through the dark matter halo [27, 28]. The highest rate is expected to be around June 2nd and smallest in December (figure 1.4). Directionality is based on the strong angular dependence of the nuclear recoils resulting from WIMP interactions [29]. The backwards scattering events will be one order of magnitude smaller than the forward ones. This directional signature allows to discriminate potential backgrounds.

The recoil energy deposited in the target material can be observed in three different signals, depending on the detector technology in use. This energy can ionise the target atoms, that release one or more electrons, produce photons via excitation and de-excitation process, or generate heat (phonons in a crystal). Experiments focus on the detection of one or a combination of two of these signals. Experiments like DAMA/LIBRA (a sodium-iodide (NaI) scintillation detector) [30] and XMASS (a liquid xenon detector) make use of the light signal. Whereas, the XENON [31] and LUX [32] experiments, also collect the charge produced during the interactions.

Given the rarity of signals produced by WIMP-nucleon interactions, it is pivotal for all the dark matter search experiments to reach very low background and to fully characterize it [33]. The leading experimental technology for direct WIMP detection is represented by a dual-phase time-projection chamber which is discussed in chapter 2. One of the most important advantages of this detector is the scalability to larger masses, which directly increases the sensitivity of the experiment.

Chapter 2

Time-Projection Chamber for Dark Matter Detection

2.1 Time-Projection Chamber

TPCs are used for different purposes and one of these is the search of signals produced by WIMPs interacting within the target region. This can be in liquid or gas phase or even both (dual-phase TPC represented in figure 2.1). By interacting, a fraction of the incoming particle's energy is transferred to the target material (section 1.3.1). Depending on the energy band of the target material, ionization electrons, scintillation photons and heat (phonons in a crystal) can be emitted. DM experiments that detect two of these signal types, looking at their relative size, are capable to discriminate nuclear recoils (neutrons, WIMP) from electronic recoils (e.g. charged particles, photon interactions) providing a strong background rejection method. Background sources are discussed in section 2.1.3. Noble-gas dual-phase time projection chambers, like the XENON experiments, described in section 2.2, are making use of the charge and light produced by incoming particles. Neutrons can elastically scatter off target nuclei transferring part of its energy to them. Through interaction with the nearby atoms, the signals described in the reaction chain represented in figure 2.2 can take place. WIMPs, are expected to interact with the target in the same way as fast neutrons (\sim MeV) do. The experiment has to be provided with a sensor able to detect the signal produced from the chosen target-material.

2.1.1 Double Phase TPC

Noble gas dual-phase TPCs are a technology that is in use for dark matter search purpose. The lower volume, the drift region, of the TPC hosts the ultra pure noble gas in the liquid state. The upper volume with the same noble element in gas phase constitutes the scintillation gap. In order to operate the TPC, electric fields have to be applied. In the liquid phase a homogeneous electric field in the $-z$ direction is applied between the cathode and gate electrodes, respectively placed at the bottom of the TPC and just under the liquid surface. A second field is applied over the liquid-gas interface between the gate and the anode, which is located in the gas phase. Signals detection processes are explained referencing to the XENON100 experiment. The light signal produced at the interaction point inside the liquid phase is called direct scintillation (S1). The XENON100 experiment is operated applying a field of 0.53 kV/cm in the liquid phase [31]. The electron produced from the ionization moves upwards with a constant drift velocity of ~ 2 mm/ μ s. Once the electrons surpasses the gate electrode, they enter in the liquid-gas interface region where a high field (~ 12 kV/cm) is present. Under the influence of this strong field, electrons are extracted from the liquid into the gas phase where they produce electroluminescence signal (S2). This signal is produced by the inelastic interaction occurring between the target atoms and the accelerated electrons. The field strength is chosen to be in the so-called *proportional mode*, in which the produced electroluminescence signal is proportional to the number of extracted electrons and, hence,

proportional to the primary ionisation in the liquid phase resulting from the detected interaction [34]. As shown in figure 2.1 on the top and bottom of the TPC arrays of photosensors are placed in order to detect the photon signals S1 and S2. From these signals the interaction vertex can be accurately reconstructed. The position information in the z axis is obtained from the relative time between the signals. Ionization electrons produced at the interaction point present small diffusion in the xy -position drifting towards the gas phase where they generate very localized secondary scintillation light (S2). The S2 signal distribution on the top PMT array can be used to determine the xy -position of the interaction point (see figure 2.1). Strong background discrimination can be applied looking at the S2/S1 ratio ($>99\%$ rejection on electron recoil) and slightly improved by looking at the S1 signal shape [35, 36]. This discrimination power of liquid xenon detectors stems from the inherent differences in ionization density along the tracks of electrons such as from gamma ray interactions versus neutrons or other nuclear recoils. The gamma rays are known to produce sparsely populated tracks [37], such that the electric field is able to more effectively strip off electrons, while alpha or neutron tracks have dense cores, which results in a high recombination rate. Electronic recoils produce a greater proportional scintillation signals (S2) than nuclear recoils.

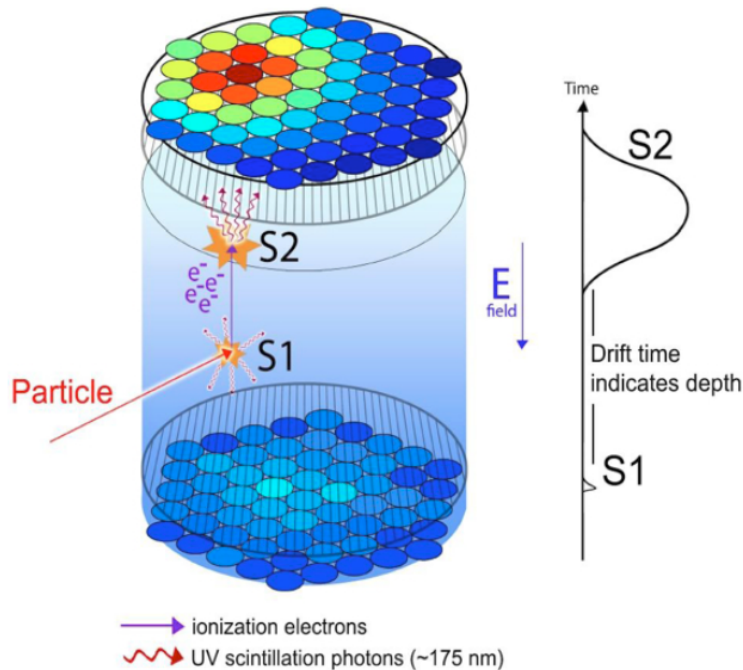


Figure 2.1: Schematic representation of a noble gas time-projection chamber. The TPC uses scintillation light (S1) and electroluminescence light (S2) to identify the incoming interacting particles. Recording these two signals from any scatter allows the vertex to be accurately reconstructed via the relative timing (position along the vertical axis) of the signals and from the hit pattern on the PMTs in the gas phase (x - y position). Additionally, from the different S2/S1 ratio produced from nuclear and electronic recoil, a strong background discrimination can be achieved. Figure from [38].

2.1.2 Noble Gas as Target Material

Suitable materials for detection of the incoming radiation have to be stable, dense, homogeneous, to not attach electrons and to be very good dielectrics. Appropriate candidates are noble gases, Xenon (Xe), Argon (Ar) and Neon (Ne) which are being used or planned to be used for dark matter direct detection. In Table 2.1 some properties of these elements are given.

Table 2.1: Physical properties of noble elements used in TPC

Properties [unit]	Xe	Ar	Ne
Atomic number Z	54	18	10
Mean relative atomic mass	131.3	40.0	20.2
Boiling point T_b at 1 atm [K]	165.0	87.3	27.1
Melting point T_m at 1 atm [K]	161.4	83.8	24.6
Gas density at 1 atm and 298 K [$\frac{g}{l}$]	5.40	1.63	0.82
Gas density at 1 atm and T_b [$\frac{g}{l}$]	9.99	5.77	9.56
Liquid density at T_b [$\frac{g}{cm^3}$]	2.94	1.40	1.21
Dielectric constant of liquid	1.95	1.51	1.53
Volume fraction in Earth's atmosphere [ppm]	0.09	9340	18.2
Peak wavelength [nm]	178	129	80
1st ionisation energy [eV]	12.1	15.8	21.6
W_{ph} in liquid for α 's [eV]	16.3, 17.9	27.1	–

Xenon Target

The use of liquid xenon as a target for DM detection is motivated by several factors:

- the outer electron shell of the noble elements is “fully occupied”, giving them little tendency to participate in chemical reactions;
- as shown in table 2.1 the density is very high allowing ton scale detectors in relatively small volumes;
- it has a high atomic number ($A \sim 131$) which increases the probability of spin-independent WIMP-nucleus interaction ($\sigma \propto A^2$);
- in gas and liquid phase it can be purified to a high level (\sim ppb impurity concentration). This is essential because, for example, water absorbs the signal photons, and electronegative impurities attach the drifting electrons. These reduce the TPC efficiency;
- it is a good dielectric.

Most of these are common also to the other noble elements mentioned. The choice of using xenon comes from its high scintillation and ionization yields, corresponding to a low 1st ionisation energy and scintillation energy W_{ph} , providing two detectable signals. The recoil energy is released by emissions of photons (scintillation) and free electrons (ionization). The de-excitation of a xenon dimer, as a consequence of an excitation or ionisation, generates photons in the vacuum ultraviolet range (178 nm) [39] (see figure 2.2). The average light yield per interaction (L_y) can then be expressed as number of photoelectrons (PE) produced per keV $_{ee}$ [40, 41]. The wavelength of the emitted photon is a further advantage of Xe with respect to Ar, since it can be detected by PMT with a synthetic silica window without need for a wavelength shifter.

2.1.3 Background Sources and Reduction Techniques

As background are defined WIMP-like events produced by non-DM particles. Given the low interaction rate of WIMPs, an ultra-low background is pivotal. There is radiation coming from the outside of the experiment, like neutrons, neutrinos and γ -rays, and radiation produced by the materials radioactivity of the experiment components themselves.

Neutrons

Neutrons, elastically scattering on xenon nuclei, produce single nuclear recoil signals which are, on an event-by-event basis, indistinguishable from a WIMP signal. This potentially dangerous

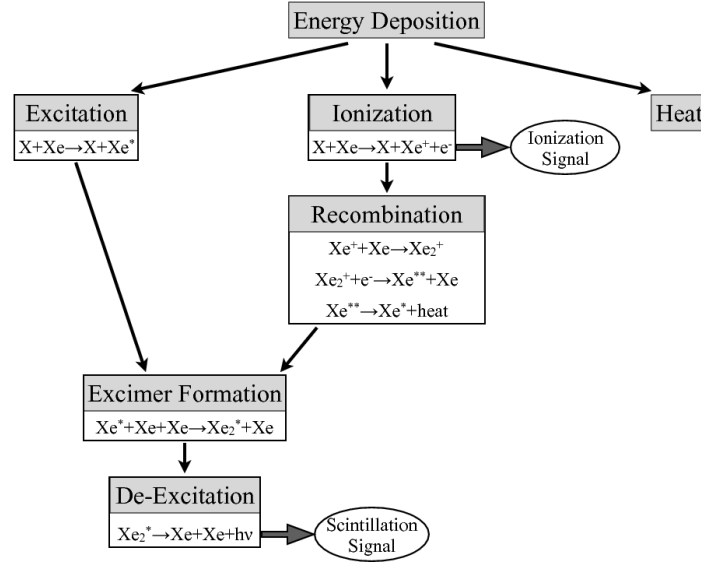


Figure 2.2: Main processes responsible for the ionization and scintillation signals in xenon. The symbol X indicates ionizing radiation. Figure from [42]

background has to be characterised and minimised. The neutrons can be of two origins: cosmogenic (GeV range) and radiogenic (MeV range). The former are induced by cosmic muons penetrating the rock into the underground laboratory. Among the different processes in which neutrons are induced by cosmic muons, *muon spallation* is the main one. This process occurs when a muon interacts with a nucleus via virtual photon producing a nuclear disintegration releasing a neutron [43]. Radiogenic neutrons, on the other hand, are produced in spontaneous fission and (α, n) reactions due to unstable isotopes such as ^{238}U , ^{235}U , and ^{232}Th .

In order to reduce cosmogenic neutron events, experiments are placed deep underground using Earth as a natural shielding against the cosmic rays. The shielding power, in order to be comparable between the different underground experiments, is given in *meter water equivalent m.w.e.* (e.g. LNGS ~ 3000 m.w.e., SNOLAB ~ 6000 m.w.e.) [44]. Furthermore, by shielding the experiment with polyethylene and/or water, having a high neutron stopping power, both neutron background source types are strongly reduced. In addition, if an experiment is shielded with a water tank, a muon veto system can be installed. This is able to tag muon and its induced showers through the detection of the Cherenkov light produced in water. The laboratories are generally located, if possible, in sites presenting a low radioactivity [45].

Neutrinos

The Sun is a strong neutrino source and a constant flux of $\sim 7 \cdot 10^{10}$ particles/cm²/s can be detected on Earth. For incoming neutrinos, with energies in the range $\sim 1 - 100$ MeV interacting via neutral current, the coherence effect takes place producing nuclear recoils with energies of a few keV [46]. Future experiments at the ton scale, due to their high sensitivity and low background, will be able to detect these neutrino interactions. The signal they produce will be a problematic background. The detection of neutrino interactions limits the sensitivity of dark matter experiments to cross-section around $\sim 10^{-45}$ cm² for WIMPs with masses around a few GeV/c². For heavier WIMPs the cross-section would be around $\sim 10^{-49}$ cm² [47]. The sensitivity of the different generation of TPCs is discussed in sections 2.2. There is no known method to block the neutrino flux crossing the experiment.

γ -rays

γ -rays are mostly produced by the decay of unstable isotopes of natural elements. Among these the most common are the isotopes belonging to the ^{232}Th and ^{238}U decay chains, the ^{40}K (primordial radionuclide) and the ^{232}Rn . Their energy can range from tens of keV up to 2.6 MeV and when interacting with matter photo absorption, Compton scattering and pair production can take place. These processes release electrons that could deposit their energies of a few keV in the target medium reducing the experiment sensitivity to dark matter events.

Surrounding the experiment by materials presenting low internal contamination, high atomic number and a high density is the best way to reduce the unavoidable gamma activity. Small experiments are predominantly shielded with a lead cover layer, whereas, big experiments prefer to place the set-up in a large water tank providing a homogeneous shield. Experiment such as XENON100, shielded with lead and copper, are flushed with pure nitrogen in order to remove the radon from the internal cavity and to prevent that the radon of the outside environment diffuses into the shielding.

Intrinsic Sources

The target material, before entering the shielded area, could suffer from cosmic activation. In case of xenon this does not present an issue. The longest lifetime of cosmic activated isotope is 36 days and belongs to ^{127}Xe [48]. This lifetime is short enough to make this isotope decay before the experiment starts. Xenon has no unstable isotopes apart from some long-lived double-beta emitters, where only the decay of ^{136}Xe has been observed with a lifetime of $2.165 \cdot 10^{21}$ years [49]. This starts to become a relevant background only for multi-ton detectors. This isotope can be removed by centrifugation.

The krypton (^{85}Kr) contamination (β -decay) of the xenon can be removed using cryogenic distillation as it has been done for XENON experiments (XENON100 krypton contamination ~ 10 atoms per trillion xenon atoms). The traces of uranium and thorium, present in all the materials, produce radon in their decay chains and this can diffuse through material and dissolve in the liquid xenon. Great efforts have to be done in order to reduce the impurities of the detector materials, and where a further reduction is not possible, a precise quantification of the background sources is needed so that they can be discriminated from the signal events during the measurements. The components of the set-up have to be screened, as it was done for XENON100 [50]. Great efforts have been made in order to reduce the radioactivity of the photomultiplier tubes dedicated to XENON1T [51].

Once the background is minimized, further strategies can be applied to improve the signal discrimination. Defining a fiducial volume, often central region of the target which most of the incoming radiation does not reach, helps to strongly reduce the γ -rays contamination. In addition, all the double scatter events are rejected, since it is not expected that a WIMP particle will interact more than once in the target volume. Once these requisites are satisfied, the signal ratio discrimination is applied (See section 2.1).

2.2 XENON Experiments

The XENON experiments XENON10, XENON100 and XENON1T are all TPC detectors designed for the purpose of WIMPs detection. To do this, the target volume has increased and the background reduced. No dark matter particle has been discovered so far, only the upper limit on the WIMP-nucleon cross-section has been improved step by step over time.

XENON10

The XENON10 (2006-2007) experiment was equipped with a 15 kg liquid xenon detector. During operation time no WIMP signatures were found, and the WIMP-nucleon spin-independent scattering cross-section upper limit was set to $5.2 \cdot 10^{-44} \text{ cm}^2$ for a 30 GeV/ c^2 WIMP mass [52].

XENON100

The XENON100 (2008-2013) has an active target of 62 kg of LXe and is surrounded by an LXe veto of 99 kg. With respect to the XENON10 experiment, the sensitivity of XENON100 is increased by ~ 50 times thanks to the ten times higher target mass and two orders of magnitude lower background. During the several runs, no dark matter signal has been observed above the expected background, leading to the most stringent limit, at the time of publication, on the spin-independent WIMP-nucleon cross-section with a minimum at $2.0 \cdot 10^{-45} \text{ cm}^2$ for a 55 GeV/ c^2 WIMP mass, based on a 225 days run [53]. A schematic view of the detector as well as a short description is presented in figure 2.3.

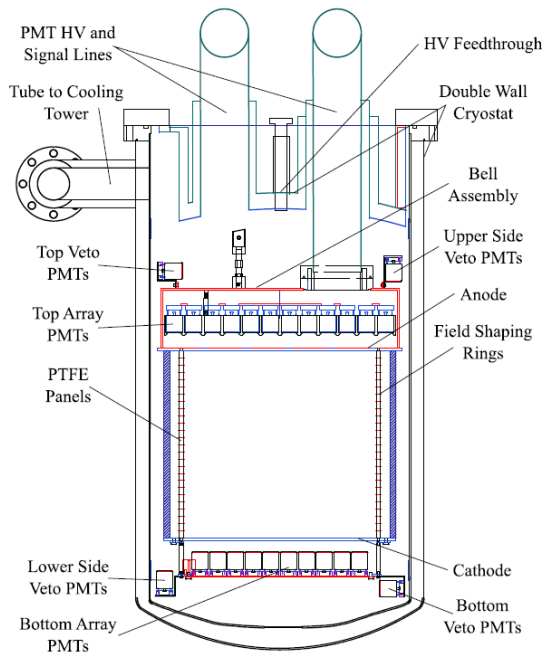


Figure 2.3: Schematic view of the XENON100 detector. The detector is being operated at Laboratori Nazionale del Gran Sasso (LNGS) since February 2008. The TPC is enclosed in a PTFE (Polytetrafluoroethylene) cylinder, made with 24 interlocking panels which support the field shaping wires. The TPC volume is closed at the bottom by a cathode mesh, and at the top by 3 meshes, a central anode sandwiched by two grounded meshes. Custom-made, low radioactivity, high voltage feedthroughs are used to bias cathode and anode. The materials used for the detector were carefully selected for having low radioactivity content, and the detector design is such that all the most radioactive components are located far away from the sensitive volume, outside the shield. The experiment has a 4π shield consisting from outside to inside of a water tanks (thickness 20 cm), a 20 cm layer of lead, 20 cm of polyethylene, and a 5 cm thick copper layer. Drawing taken from [31].

XENON1T

The XENON collaboration has worked on the next phase, XENON1T, whose target volume contains ~ 2 ton of ultra radio-pure liquid xenon [54]. This experiment is also conducted at the Gran Sasso Laboratory. The construction of this new detector started in 2013 and ended in 2015. The cryostat vessel containing the xenon is housed in a 10 m diameter and 10 m height water tank that serves as a muon veto [55]. The predicted sensitivity at 50 GeV/ c^2 is $1.6 \cdot 10^{-47} \text{ cm}^2$ for a two ton \times years exposure [56]. In about 2 (5) days it is expected to achieve the sensitivity of the XENON100 (LUX) experiment.

2.2.1 DARWIN

The DARWIN (dark matter wimp search with noble liquids) experiment, a 50 tons xenon TPC with a fiducial mass of ~ 30 t, aims to reach a sensitivity to spin-independent WIMP nucleon cross-sections around $2.5 \cdot 10^{-49} \text{ cm}^2$ [57], two order of magnitude lower than the next generation experiments such as XENON1T, DarkSide, and SuperCDMS [58]. A collection of sensitivity levels achieved by performed experiments and the goals of the next planned ones are represented in figure 2.4. The size of the detector together with the low aimed background, enables DARWIN to detect

solar pp-neutrinos and ${}^7\text{Be}$ -neutrinos and also the search for neutrinoless double beta decay of ${}^{136}\text{Xe}$. From the simulations performed, considering a fiducial volume of 14 tons and 5 years of data, around 5900 pp-neutrino events are expected [57]. Concerning the neutrinoless double beta decay an improvement of the sensitivity to $T_{1/2}^{0\nu} = 5.6 \cdot 10^{26} \text{y}$ corresponds to a lower limit on the half-life increased by more than a factor 20 with respect to the current lower limit presented by EXO-200 [59] and KamLAND-Zen [60].

Extraordinary Low-background Requirements

Even if the PMTs have been optimized for use in xenon based experiments and for low radioactivity, they suffer from relatively large size and constitute an important source of intrinsic ER background (see section 2.1.3) in the XENON100 and XENON1T experiments [56]. PMTs have been developed to be operated in extremely low light level condition, in which they are capable of single photon counting. Under these condition the signal output they provide is directly proportional to the number of photons in the incident light signal. Unfortunately this linearity is lost when operated at higher signal rates and for high energy interactions. Since calibrations are performed with radioactive sources, which signals are detected in the non-linear region of the PMTs, the precision of position and energy reconstruction is limited. To overcome these problems new semiconductor photosensors such as avalanche photodiode and multi-pixel photcounter have been investigated as part of this thesis (see Chapter 4). Semiconductor photodetectors present a much higher detecting surface to mass ratio and have a low associated radiation that would only add a small contribution to the overall intrinsic background. They could be a sensor for future xenon-based experiments in the field of solar neutrino and direct dark matter searches, and double beta decay studies [61].

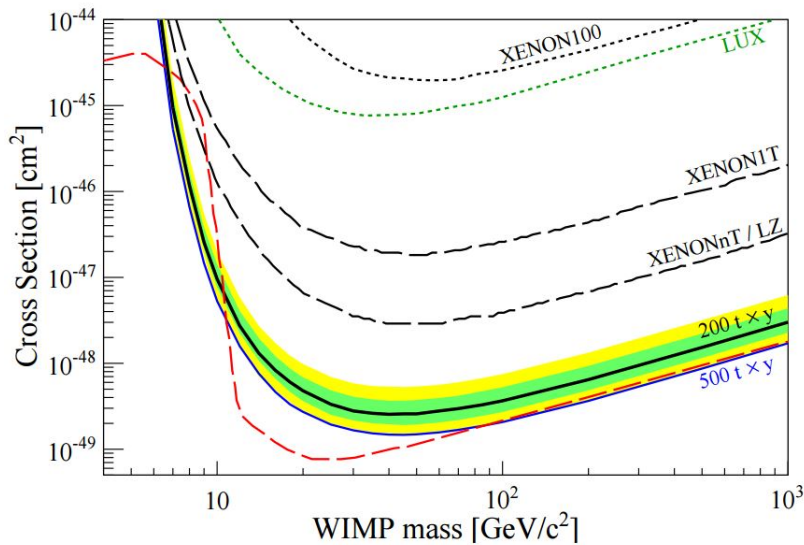


Figure 2.4: Collection of the upper limits set to the WIMP-nucleon spin-independent scattering cross-section, related to the WIMP mass, achieved by the XENON100 and LUX experiments, and the projected sensitivity the XENON1T. Also represented is the sensitivity for multi-ton LXe detectors (with exposure $200 \text{ t} \times \text{y}$ (black, with $1\sigma/2\sigma$ intervals) and $500 \text{ t} \times \text{y}$ (blue)) determined using a likelihood analysis assuming a $5\text{-}35 \text{ keV}_{nr}$ energy interval, a separation of the electronic and nuclear recoil distributions corresponding to 99.98% electronic recoil rejection at 30% nuclear recoil acceptance, and a combined energy scale with $L_y = 8.0 \text{ PE/keV}_{ee}$. The multi-ton detectors are designed to probe the entire parameter region for WIMP masses above $\sim 6 \text{ GeV}/c^2$, until the neutrino background (red dashed line) will start to dominate the recoil spectrum. Figure from [62].

2.3 Overview of the MarmotXL TPC Project

2.3.1 TPC for MarmotXL

With the purpose of identifying a new suitable photodetector (PD), satisfying the extremely low background requirements of the future xenon-based experiments such as DARWIN (section 2.2.1), a hybrid TPC with a top array including different types of PD has been studied. The work performed with the 1-inch PMT and the Multi-Pixel Photon Counters (MPPC) is presented respectively in chapter 3 and chapter 4. The study of the top array geometry is presented in chapter 5. This TPC will not only be used for the study of new PDs but will also provide a suitable set-up for studies of the drift and extraction fields. Furthermore, the TPC will be used to improve the position reconstruction at energies above ~ 1 MeV and allow the study of double-beta decay. The signals S1 and S2, as described in section 2.1.2, are detected by two arrays of PDs located at the top and bottom of the TPC. The TPC will be hosted in MarmotXL, a cryostat built for photodetector testing in a liquid xenon environment. A schematic view of the TPC main components is shown in figure 2.5.

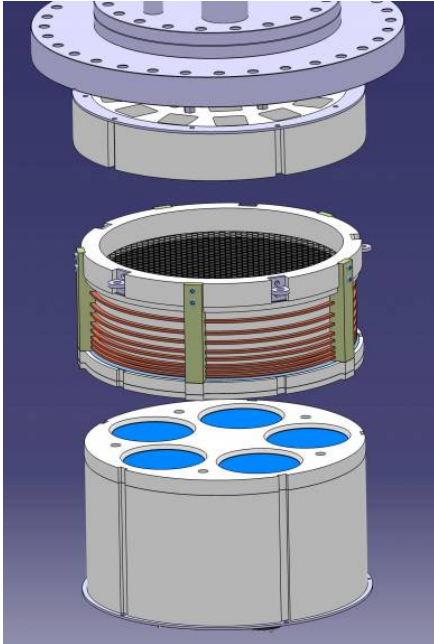


Figure 2.5: Technical drawing of the TPC. The PTFE filler at the bottom, hosting the lower PD array, is used to reduce the amount of xenon needed in order to reach the operation level. In the central part the shaping rings, used to produce a homogeneous field inside the chamber, are visible, as well as the anode and gate grids. At the top the second PD-array holder is shown.

2.3.2 MarmotXL

MarmotXL was designed and built at the University of Zurich (figure 2.6) and is mainly used for testing the PDs for the XENON experiments [53]. MarmotXL is a cryostat that allows the operation of multiple PD at temperatures at which the xenon is in the liquid phase (-100 °C), and absolute pressures up to 2 bar can be reached. In order to improve the thermal insulation of the cryostat heat transfer between the inner and the outer vessel has to be limited. By strongly reducing the pressure (10^{-6} mbar) of this region the thermal conduction in air (diffusion and collisions of particles or quasi-particles within a body due to a temperature gradient) is drastically reduced. To reduce the thermal radiation the inner side of the outer vessel is lined with aluminium-tape, and the outside of the inner chamber is wrapped with a mylar multilayer insulation (10 layers) in order to reflect the radiation incoming from the outside. The same multilayer insulation is positioned on the bottom-plate. This thermal insulation improvement increases the pumping time required to obtain the vacuum, as there is out-gassing coming from the adhesive of the tape used to fix them [63].

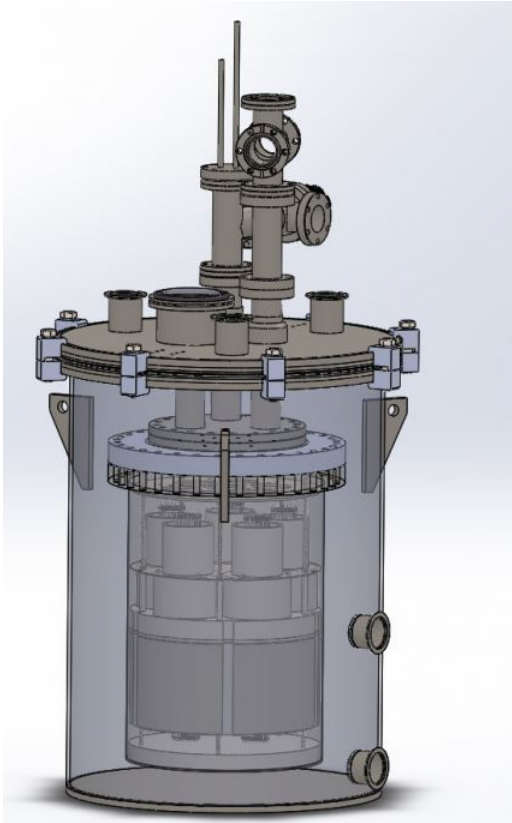


Figure 2.6: Technical drawing of the MarmotXL, a cryostat consisting of two vessels one inside the other. The internal vessel hosts the tested photodetectors which are in contact with the liquid xenon. As represented, the feedthroughs are placed on the top of the set-up, where also the Pulse Tube Refrigerator (PTR), providing the stable cooling power, is located. The pumping ports are situated on the side of the outer vessel. In order to be operated the cryostat is connected to the gas system that is responsible for the recirculation and purification of the xenon gas. The drawing shows the inner chamber hosting 10 3-inch PMTs facing each other.

MarmotXL is supported during operation by a slow control system and an emergency cooling system. The former, as described in section 4.2.2, is used for monitoring and recording the data of the experimental conditions such as pressure and temperature. Furthermore, safety regions can be set for the measured parameters. If the safety region is exceeded the alarm is triggered. As an example, in this case when a pressure higher than 2.5 bar is measured, in order to prevent serious damage to the instrumentation, the emergency cooling system is triggered. The emergency cooling system is an essential part, preventing explosion or damage to the cryostat chamber in case of a failure of the primary cooling system, which would cause a pressure rise above the safety conditions. In case of a failure, liquid nitrogen with a gauge pressure of 1-3 bar flows through copper brackets attached to the gas system pipes inside the outer vessel. Reducing the inner vessel temperature the pressure decreases.

2.3.3 Photodetectors

The new TPC makes use of two PD types: vacuum photomultiplier tubes and silicon PDs. Of the former, a 3-inch model will be used for the bottom PD array and an 1-inch model as part of the top array. A description of the 1-inch PMT (model R8520-406) and the tests performed, in order to characterize the gain of these PMTs, is given in chapter 3. For the silicon-based PDs, two models are implemented on the top array, the Avalanche Photodiode (APD), previously characterised [64], and the MPPC. The latter, whose characterisation was part of this thesis, is described in detail in chapter 4, and the results of the first tests at room temperature are presented.

2.3.4 Design and Simulation

In a xenon dual-phase TPC the information about interaction of incoming particle with the target is obtained through the collection of the photons constituting the S1 and S2 signals. It is pivotal to have a high Light Collection Efficiency (LCE), this refers to the percentage of photons produced

that are detected. The LCE is influenced by the materials used for the construction of the TPC, the purity of the xenon, the size and geometry of the chamber, and the geometry and detection efficiency of the PD arrays. The performed simulations investigating the most appropriate TPC geometry are described in chapter 5. The electric field is produced and made homogeneous by the meshes inside the chamber and the shaping rings placed around the outer wall of the TPC. In total the use of 5 meshes is planned, two in order to reduce to zero the field in the PD areas to guarantee a correct performance, called bottom and top screening meshes. The relevant detection area is the one between the cathode and gate grid, producing the drift field in the liquid phase. The anode mesh is placed in the gas phase just above the gate. This is used to generate the strong extraction field (section 2.1). The study of the electric field inside the chamber is not part of this thesis.

Chapter 3

Photomultiplier Tube

A PD candidate for the MarmotXL TPC is the Hamamatsu 1-inch PMT model R8520-406. The working principle of a PMT and the characteristics relevant to this work are presented in section 3.1, whereas a complete description can be found in [65]. Hamamatsu provides a data sheet with the values measured just for a subset of the PMTs of the same type. Not every PMT presents exactly the same properties, so the gain vs HV were analyzed in the laboratory for each of the 23 PMTs (list given in table 3.1).

This chapter is divided into three main parts. Section 3.1 presents a short overview of the basic properties characterizing PMT, in order to provide a better understanding of the data obtained during the tests. The description follows the Hamamatsu handbook [65]. In chapter 3.3 the two used set-ups and the readout electronics are discussed, as well as the timeline of the performed tests. In chapter 3.5 the data collected are presented and discussed.

Table 3.1: Tested PMTs, model R8520-406, sorted by serial number. One older PMT (serial number ZA2352) was characterized as well.

LV1032	LV1036	LV1041	LV1068	LV1076	LV1154
LV1033	LV1037	LV1042	LV1070	LV1079	LV1155
LV1034	LV1038	LV1046	LV1074	LV1080	LV1163
LV1035	LV1040	LV1067	LV1075	LV1153	ZA2352

3.1 General Description

PMTs are vacuum tubes working as very sensitive light detectors over a very wide wavelength range, going from ultraviolet to the near-infrared. The tube (Figure 3.1) has an input window that is a transition mode photocathode where electrons are emitted via the photoelectric effect, these are called *photoelectrons*. These follow the electric field generated by the focusing electrode and the dynodes, onto the first dynode where they are multiplied by means of secondary electron emission. This multiplication process takes place at each of the N dynodes. This avalanche process ends at the anode, where the charge current produced is read out. On the back part of the PMT case, there are 23 pins, to which a base is attached. The base has the function to subdivide the high voltage (HV) and provide the proper voltage gradient to each dynode. This is possible thanks to the resistor and capacitor mounted on the *Cirlex* board [66]. These also allows to transform the electron current signal, produced by the PMT when operated, into a voltage signal. The bases used during the measurements have to same design as the one used in the XENON100 experiment.

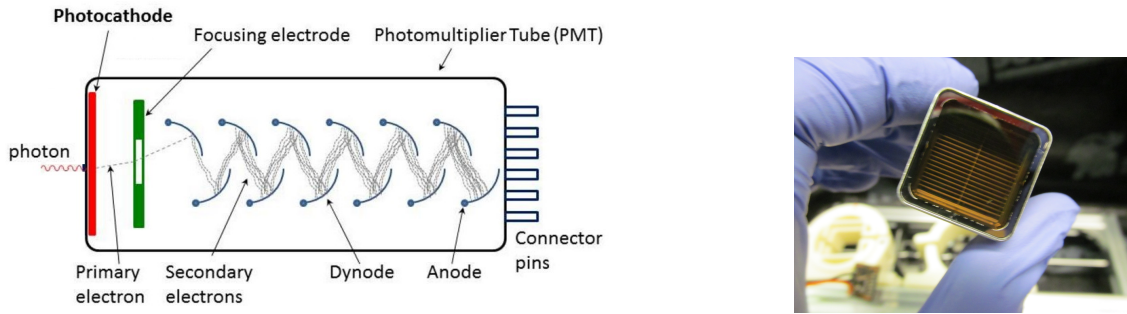


Figure 3.1: (left) Representation of the basic elements which constitute a PMT. Figure from [65]. (right) Photograph of the front window of a PMT model R8520-406.

3.1.1 Quantum Efficiency

The energy carried by the incident photon is converted into photoelectrons when interacting with the photocathode material. The conversion efficiency (photocathode sensitivity) varies with the incident light wavelength. This relationship between the photocathode and the incident light wavelength is referred to as *the spectral response characteristics*. This can be expressed in terms of quantum efficiency (QE). The QE of a PD is the ratio between the number of photoelectrons emitted from the photocathode and the number of incident photons. It is denoted by η and is generally expressed in percent units. The incident photons transfer their energy to electrons in the valence band of a photocathode. Photons at shorter wavelengths carry higher energy compared to those at longer wavelengths and contribute to an increase in the photoemission probability. The window material has to be carefully chosen in order to be transparent to the wavelengths that have to be detected.

3.1.2 Dark Counts

Under the influence of the electric field an electron in the valence band of the photocathode can be subject to thermionic or field emission. The released electron is then accelerated onto the first dynode where it starts the avalanche process. The signals produced are identical to the ones obtained by the detection of one photon. These signals are called *dark counts*, and the number of such signal over time is the *dark count rate*. One hour before start taking data it is strongly recommended to already apply the operation voltage to the PMT (warm-up the PMTs). This stabilizes the dark count rate, which initially can be very high. The thermionic emission contribution to this effect. This is reduced by 3 to 4 order of magnitude when the PMT is operated at low temperature such as in liquid xenon compared to room temperature.

3.1.3 Afterpulse

A signal, produced by photoelectrons, presenting some delay with respect to the main photoelectron peak is called *afterpulse*. The pressure inside the PMT is around 10^{-6} Pa. Therefore, it can happen that a single gas atom is hit and ionised by a photoelectron or one of the secondary electrons. This positive ion, flying in the opposite direction with respect to the electrons, could produce a signal, identical to a single photon signal, by hitting the photocathode. These signals with a few μs delay are very unpleasant in low light application such photon counting. The rate of these afterpulses depends on the vacuum quality and increases by vacuum degeneration. This can be an effect of leaks, outgassing of the internal components and infiltration of environment gases by diffusion. Signal with a few ns delay can be produced by electrons that scatter away from a dynode. After that, following the electric field to a dynode, they start a new avalanche process. The pulses produced by these electrons are so near to the signal peaks that resulting signals are often a sum of the main and these afterpulses peaks.

3.1.4 Gain (Current Amplification)

The number of secondary electrons released at each dynode is related to the potential difference V_i between the dynodes, and a material constant k that can be between 0.7 and 0.8. The emission ratio δ is:

$$\delta = a \cdot V_i^k, \quad (3.1)$$

where a is a constant. The photoelectron current I_{pc} , released at the photocathode by an incident photon, once it reaches the first dynode is amplified by a factor δ_1 , at the second dynode again by a factor δ_2 , and so on. The current I_a that reaches the anode after a number of stages equal to n will be:

$$I_a = I_{pc} \cdot \alpha \cdot \delta_1 \cdot \delta_2 \cdots \delta_n, \quad (3.2)$$

where α is the collection efficiency, given by the fact that some electrons are lost from stage to stage. The gain μ is obtained from the ratio between I_a and I_{pc} . Combining all the information and assuming $\alpha = 1$ and an operation voltage V equally divided over the n stages ($V_i = V_j$), the following expression is obtained;

$$\mu = \frac{I_a}{I_{pc}} = \alpha \cdot \sum_{i=1}^n \delta_i = (a \cdot V_i^k)^n = a^n \left(\frac{V}{n+1} \right)^{kn} = A \cdot V^{kn}, \quad (3.3)$$

where the constants $(a^n)/(n+1)^{kn}$ are combined into A . The gain expressed in this form is clearly proportional to the kn exponential power of the supply voltage. In the presence of n dynodes, between photocathode and anode there are $n+1$ potential difference steps.

3.2 Model R8520-406

The R8520-406, shown in figure 3.2, is a one square inch PMT presenting all the important features for use in liquid xenon. The PMT has a 20.5×20.5 mm² minimum effective photocathode window made of synthetic silica that has a high level of transparency ($\sim 80\%$) to the wavelength of LXe scintillation (178 nm). The quantum efficiency of this PMT model has a maximum of $\sim 30\%$ at a wavelength of 178 nm. Bialkali photocathodes are frequently used for scintillator application, since they have a spectral response which fits the emission spectra of most scintillators. These PMTs have 10-dynodes and a linear-focused style dynode structure, with the feature of a fast time response and high pulse linearity. This dynode structure gives a typical gain of $\sim 10^6$ when negatively biased with an operation voltage of 800 V. The maximum voltage applicable between anode and cathode without damaging the PMT is 900 V [67].



Figure 3.2: Photo of a 1-inch PMT model R8520-406. Visible are the synthetic silica window, the cobalt-free metal case and at the bottom two of the 23 pins on which the base is attached.

3.3 Gain Measurements

3.3.1 General Set-up Requirements

To perform the tests a light-tight environment is needed. Two different set-ups were used to collect data: the Black Box (BB) and the SandBox described in section 3.3.1 and 3.3.1. Inside both set-up a blue Light Emitting Diode (LED) has been placed. The electronic components used to execute the measurement are described in section 3.3.2.

Black Box

This is a black plastic box, in which a LED ($\lambda = 470 \mu\text{m}$) is present. The BB is used to perform tests at room temperature and pressure. In order to minimize the influence of external light, the black box is wrapped with a thick black cloth and then wrapped in an aluminum cover that reflects the external light.

SandBox

The SandBox is a new (2014) equipment designed and built by Sandro D'Amato as part of his Bachelor thesis [68]. The motivation behind the realisation of this facility was the characterisation and the study of photocathode uniformity of XENON dedicated PMTs. SandBox provides a dark environment for the PMTs being tested, and includes hardware that allows to perform the measurements fully automatically. As shown in figure 3.3.1 the box is provided with a XY-Table that allows the light source to be moved remotely, thanks to a stepper motor, with a position resolution of $15 \mu\text{m}$. During the realisation of this set-up, different supports for 3-inch and 1-inch PMTs have been built. The light source in this set-up is located in an aluminium box with a collimator on the top. SandBox is provided with all connectors needed to test up to 8 PMT at the same time.

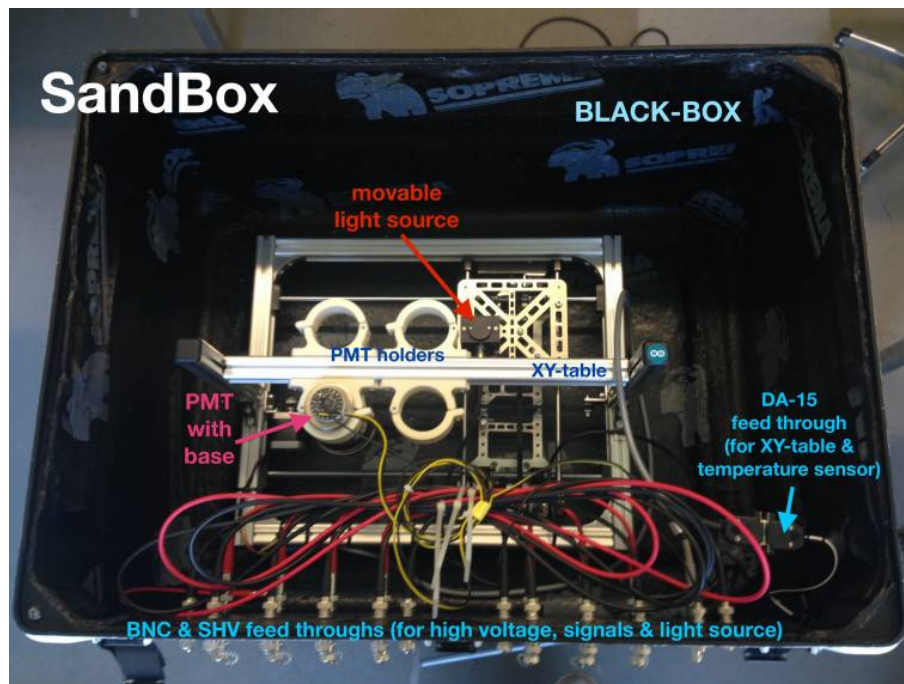


Figure 3.3: Inside of the SandBox with the most important parts labeled, and one 3-inch PMT installed. Figure from [68].

3.3.2 Electronic Equipment

In order to operate the PMT, a high voltage (HV) power supply which allows to set the high voltage separately for each PMTs is used. The power supply (CAEN Mod. N1470) returns information about the flowing current and allows the setting of a maximum current that, if reached, causes the high voltage to be switched off in order to prevent damage to the PMTs. The LEDs inside the two boxes have been powered with a Direct Digital Synthesis (DDS) Function Generator, providing NIM signal that has been used as trigger for gain measurements.

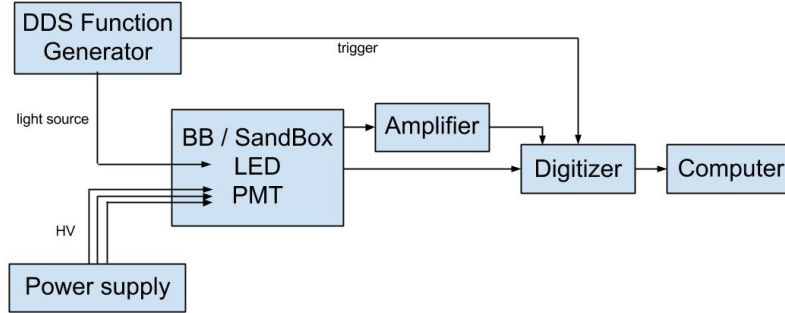


Figure 3.4: Schematic representation of the experimental set-up.

All the cabling has been kept as short as possible to prevent noise pick-up. In figure 3.4 the schematic of the electronics chain is depicted. Some of the measurements have been performed using an amplifier, realized by the electronic workshop at the University of Zurich. It has an amplification factor of $\times 10$ when powered with 10 V, with a linear amplification and low noise level. In order to reduce the noise that can be picked-up, the amplifier has been installed in an aluminum box. Signals have been digitized using a CAEN V1724 Flash Analog-to-Digital Converter (FADC).

3.3.3 Data Acquisition and Processing

Data Acquisition

The analog (voltage) signal produced from the PMT, coupled with the base, is transported through cable to the electronics instrumentation. The signal is digitized in order to be readable for the computer. An ADC is a device that converts a continuous physical quantity (usually voltage) to a digital number that represents quantitatively amplitudes. A waveform corresponds to finite duration subset of analog signal converted to digital values. A typical waveform recorded with a PMT in BB / SandBox is shown in figure 3.5, and the digitizer parameters are:

$$\begin{aligned} 1 \text{ ADC sample} &= 10 \text{ ns}; \\ 1 \text{ ADC count} &= 0.1373 \text{ mV}. \end{aligned} \tag{3.4}$$

The value of 1 ADC count is obtained dividing the maximal range of 2.25 V by 2^{14} , corresponding to the 14 bit resolution.

During every measurement, 0.5 or $1 \cdot 10^6$ waveforms have been acquired. Using a pulse generator that provides also a trigger signal the acquisition rate can be set manually. Using waveforms of $5 \mu\text{s}$ and the trigger rate kept under 3 kHz, only one signal per waveform was present in the signal region, as shown in figure 3.5.

Data Processing

Once the waveforms are collected, the data can be used to obtain a spectrum like in figure 3.6. The processing program is structured in the following parts:

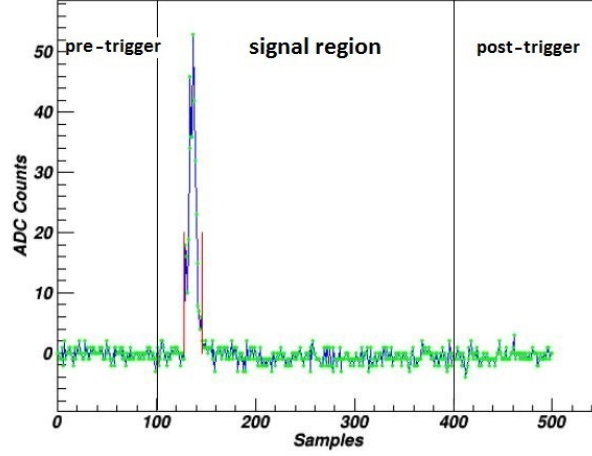


Figure 3.5: $5\ \mu\text{s}$ long waveform with a significant peak corresponding approximately to $7.4\ \text{mV}$. The pre-trigger and post-trigger regions are used to define the baseline.

- All the data of the waveform are read in.
- The baseline noise is calculated from the standard deviation in the value of the first and last hundred samples in every waveform. This can be done since the signal peak is kept in the signal region.
- The program sets a threshold of 3σ above the noise level. When a set of subsequent ADC samples have an ADC count above this threshold, their values are added together. This corresponds to the *integrated ADC counts* ($\text{V}\cdot\text{s}$).
- The spectrum is obtained by binning the integrated ADC counts in ADC channels defined in equation 3.5.

The program calculates the area taking into consideration up to three ADC samples on both sides of the subset. This is done in order to add the contribution of the rising and falling signal tail below the 3σ threshold.

The expression given in equation 3.5 corresponds to one integrated ADC channel. V stands for voltage and can be expressed as the resistance R multiplied with the current I , and in turn, the current is given as charges Q per unit time t :

$$1\text{ADC count} \times 1\text{ADC sample} = V \times t = (RI) t = \left(R \times \frac{Q}{t}\right) t = R \cdot Q \quad (3.5)$$

The whole electronic system has the same impedance value in order to avoid overshoot and unwanted oscillation of the signal (signal ringing). Impedance matching maximizes the power transfer or minimizes signal reflection when moving from an electrical load to another. The impedance of a resistor corresponds to its resistivity. The electronic set-up impedance match has been obtained by installing a $50\ \text{Ohm}$ resistance R on the PMT base. Rearranging equation 3.5, Q is found to be:

$$Q = \frac{1\text{ADC count} \times 1\text{ADC sample}}{R} = 2.7466 \cdot 10^{-14} \frac{\text{V} \cdot \text{s}}{\Omega}. \quad (3.6)$$

Dividing this charge amount by the elementary charge ($e = 1.6 \cdot 10^{-19}\ \text{C}$), the number of electrons corresponding to one ADC channel is found, making it possible to characterize the obtained spectra:

$$\frac{Q}{e} = \frac{2.7466 \cdot 10^{-14}}{1.60217657 \cdot 10^{-19}} = 1.71429 \cdot 10^5. \quad (3.7)$$

3.3.4 Gain Measurement

The gain of a photodetector describes its amplification power related to the outgoing signal compared to the incoming one. This property can be characterised, for a given voltage, by performing low light level measurements (single photon detection). Processing the data obtained as described in section 3.3.3 a single photon spectrum is obtained (see figure 3.6). An optimal spectrum presents two peaks; at low integrated ADC counts a peak produced by the noise higher than the set threshold, followed by the single photoelectron peak. Some spectra show also a third small double photoelectron peak. In the spectrum shown in figure 3.6 the presence of the first two peaks is clear, but the last one is only recognised by the fitting program. The fit on the data is obtained by summing up three Gaussian functions as given in the following equation:

$$f(x) = a_n \cdot \text{Gauss}(\mu_n, \sigma_n) + a_{SPE} \cdot \text{Gauss}(\mu_{SPE}, \sigma_{SPE}) + a_2 \cdot \text{Gauss}(2\mu_{SPE}, \sqrt{2}\sigma_{SPE}). \quad (3.8)$$

The parameters of the third Gaussian are correlated to the ones describing the single photoelectron signal since this is produced by two of them occurring at the same time.

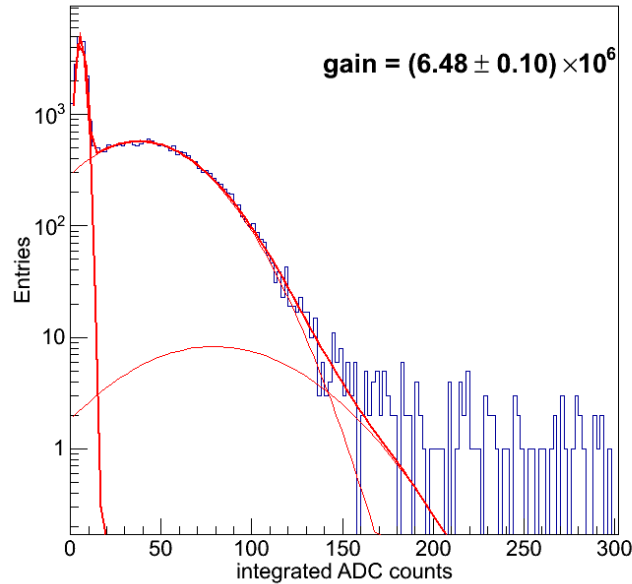


Figure 3.6: Spectrum obtained with PMT LV1032 powered with 900 V and using the LED as light source. The fit on the data has been obtained using three Gaussian functions.

The single photoelectron (SPE) signal is described by the second Gaussian, and its expectation value (μ_{SPE}) corresponds to the number of electrons obtained at the end of the avalanche multiplication. Knowing this parameter, and assuming that one photoelectron is released by one photon interacting with the photocathode, the gain is obtained by multiplication of the μ_{SPE} with the result obtained in equation 3.7:

$$\text{Gain} = \mu_{SPE} \cdot 1.71429 \cdot 10^5. \quad (3.9)$$

If an amplifier is used, the result of equation 3.9 must be divided by the amplification factor in order to obtain the gain of the photodetector.

3.4 Measurements Time Line

3.4.1 Black Box

First Run

During the first data collection no amplifier was used and the main task was to set up the electronic instrumentation. The LED is adjusted to provide the correct amount of light when the DDS function generator provides a rectangular pulse with an amplitude of $+(2.10-2.30)$ V, a pulse width of 50 ns and a pulse period of $5 \mu\text{s}$. The blue LED ($\lambda = 470$ nm) has been covered by PTFE tape, in order to diffuse the light and have homogeneous light distribution. As shown in figure 3.7 the BB was organized in order to allow to test three PMTs at the same time.

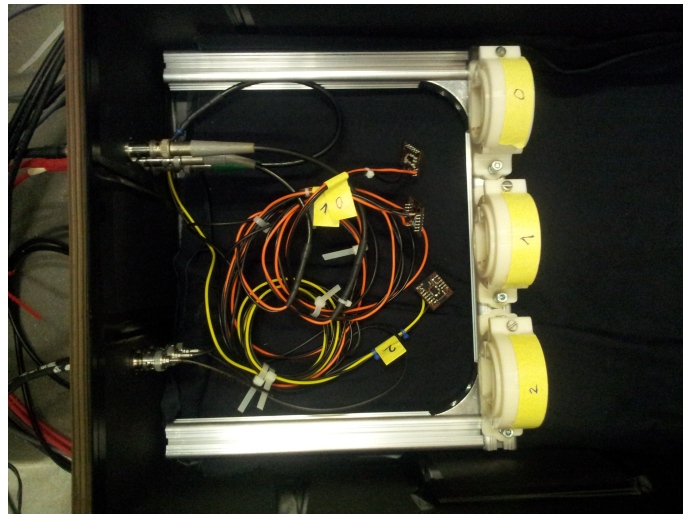


Figure 3.7: The three holders and the corresponding bases with HV and signal cables are shown inside the BB. The LED is fixed on the opposite wall.

During the first measurement one of the PMTs was tripping at voltage higher than 700 V. Observing this behaviour using the same base with other PMTs, the problem was attributed to the base. After fixing the electronic circuit the base was able to support HV up to 900 V.

Second Run

Using the previous set-up, the effects of using an amplifier have been studied. Using the amplifier, realized at the University of Zurich, the gain calculation resulted to be easier since the separation between the noise and the SPE signal was clearer. This separation also allowed to obtain the gain at lower HV settings. In figure 3.8 a comparison between the spectra taken at two different HV during the first and the second run is presented. This is the reason why all subsequent measurements were performed using an amplifier.

3.4.2 SandBox

A second measurement campaign was performed using the SandBox. For the gain measurements, the collimator on the light source was removed in order to irradiate the three PMTs at the same time. The noise level was much lower in the SandBox than in the BB. Given that, clear spectra were obtained using SandBox, all the PMTs were tested again. In figure 3.9 the strong noise reduction is visible.

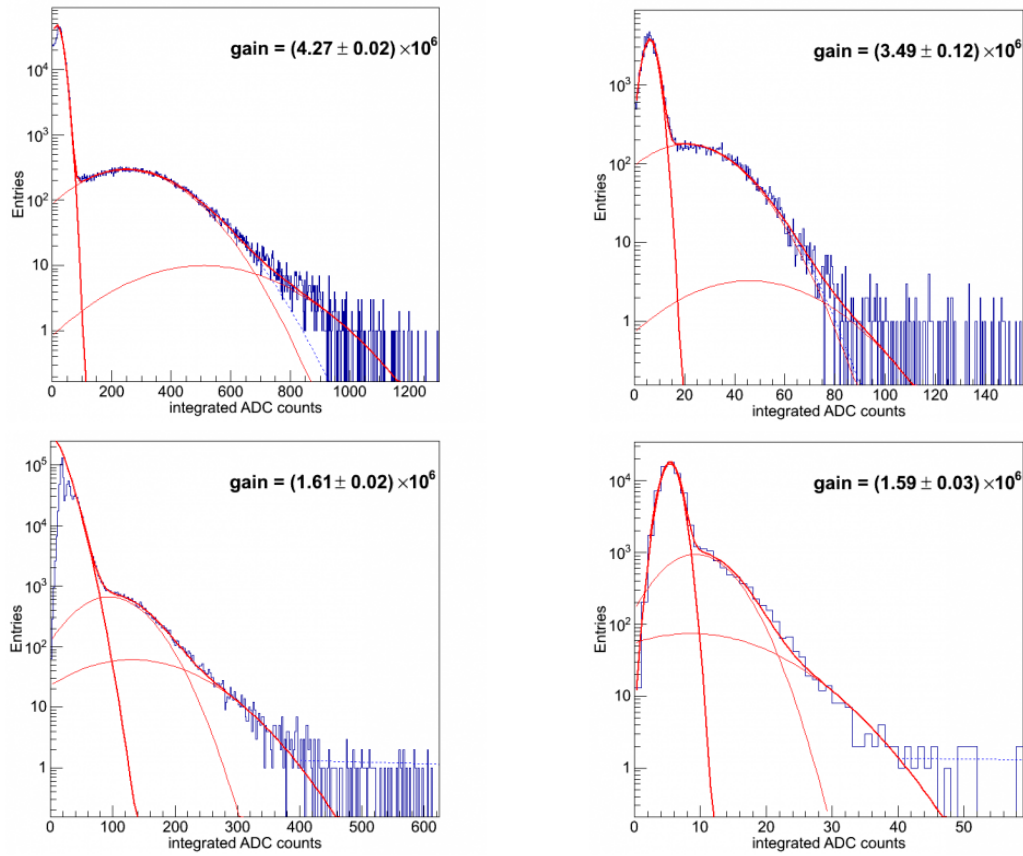


Figure 3.8: Spectrum obtained for PMT LV1067 whit (left coloumn) and without an amplifier(right column) at a voltage of 850 V (first line) and at 750 V (second line). The discrepancy between gains in the first line arise from the fact that without amplifier it resulted impossible to obtain a good fit. Using an amplifier, the signal to noise ratio improved, which allows to define the gain also at lower voltages. For the gain calculation the amplification factor has already been considered.

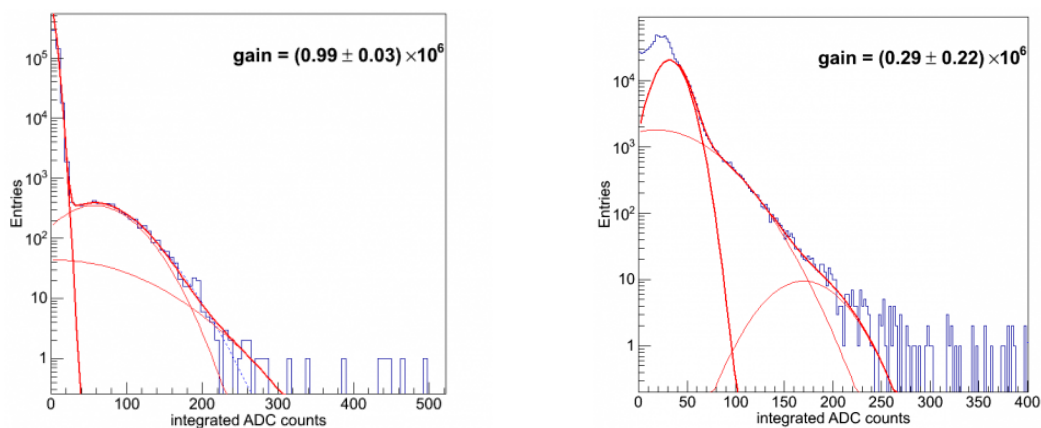


Figure 3.9: The noise inside the SandBox (left) is about three times smaller than inside the BB (right). This strong reduction allows to obtain a precise gain measurement also at a voltage of 700 V as shown here for PMT LV1033.

3.5 Results and Conclusions

3.5.1 Gain HV Dependency

Given the accurate signal peak identification obtained using SandBox, compared to BB, only the data obtained from it have been used to draw conclusions. Figure 3.10 shows a collection of all the gain measurements obtained using an amplifier. The measurements have always been done starting at 900 V and then lowering the voltage to reach 700 V, corresponding to the lowest voltage at which it was still possible to characterise the gain. The gain values are in the range given for this model from Hamamatsu.

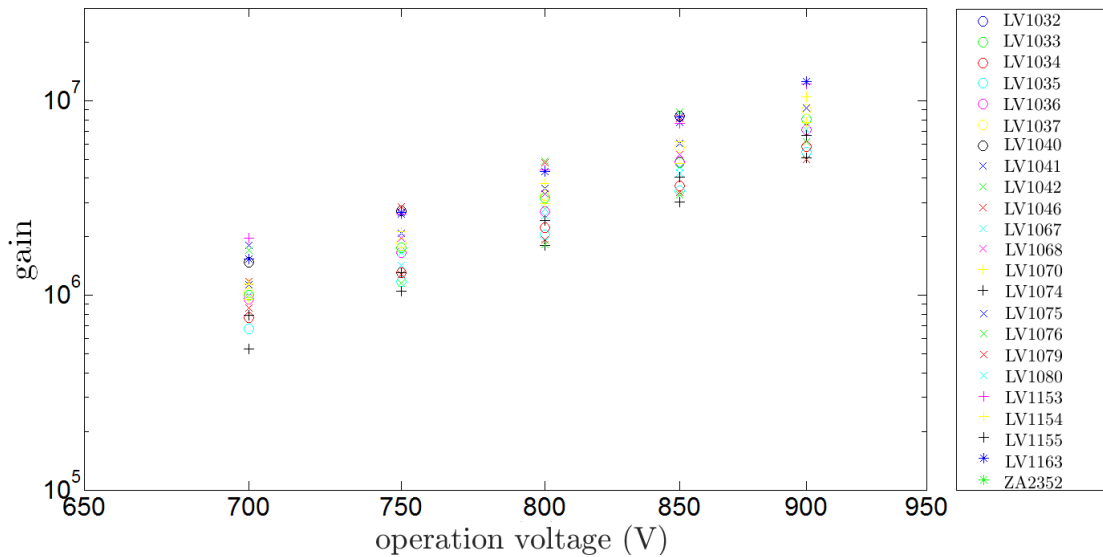


Figure 3.10: Collection of all the gain measurements performed with SandBox given in semi-log scale. The error bars have been omitted given the number of overlapping data points.

If the gain has to be characterized for voltage lower than 800 V at room temperature, the use of an amplifier is recommended.

Figure 3.11 shows the data collected for two PMTs with and without an amplifier. At the lowest gain measurements, obtained without the amplifier, both PMTs show a discrepancy with the data obtained using the amplifier. Except for PMT LV1032 at 850 V, at higher operation voltages this is not the case. The gain obtained without amplifier are within the error bars of the measurements taken using the amplifier. The discrepancies arise from the fitting program, misidentifying the expectation value μ_{SPE} of single photoelectron peak vanishing into the noise peak (see figure 3.8).

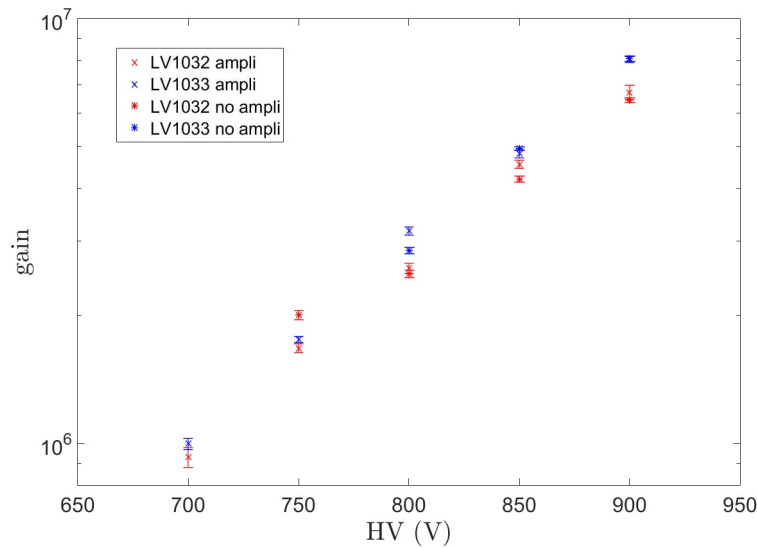


Figure 3.11: Gain results at different HV for PMT LV1032 and LV1033 using an amplifier and not using it represented in a double log scale. At room temperature without an amplifier it was not possible to identify the gain at a HV below 800 V. The error bars correspond to the standard deviation of the individual measurements.

3.5.2 Resolution

Given the good spectrum obtained during the test in SandBox also the resolution on SPE has been computed. This is obtained dividing the width of the single PE peak (σ_{SPE}) by its expectation value (μ_{SPE}). Lower resolution means that the SPE peak identification is clear. The correlation

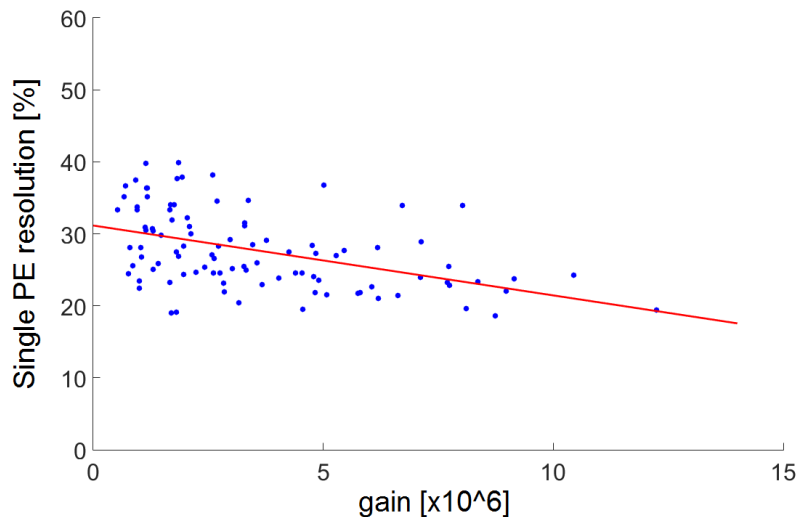


Figure 3.12: Represented is the correlation between resolution and the gain of all tested PMTs.

between resolution and gain represented in figure 3.12 shows that the resolution improves at higher gain. The same PMT model has been analysed for the XENON100 experiment [69]. Similar distribution and mean value (red line in figure 3.12) have been obtained for the resolution gain correlation.

3.5.3 Conclusions and Outlook

The gains have been characterized for twenty-two PMTs model R8520-406, and the PMT LV1038 was found to be broken. A small program has been written in Matlab that fits the collected data. The behaviour of the gain, with respect to the operation voltage, is in agreement with the HV dependency given in equation 3.3 as shown in figure 3.13. The fits have been used to define the parameters k and A given in equation 3.3. With these parameters the program returns the needed voltage in order to get a required gain.

It has been found that the k value of all the PMT ranges between 0.8 and 0.86. This is slightly higher than the values given by the general Hamamatsu PMT handbook [65]. The k value for this model has not been provided but as shown in figure 3.13 the fits describe well the data. The gain of the PMT is not influenced by the temperature [63], so the obtained results can directly be used when the TPC will be operative. Table 3.2 presents the HV required for every single PMT in order to provide a gain of $2 \cdot 10^6$. Thanks to the good resolution (20-40%) and the high gain this model is a valid candidate for the TPC project. Next step, once the TPC is built, is to test the performance of the PMTs in LXe.

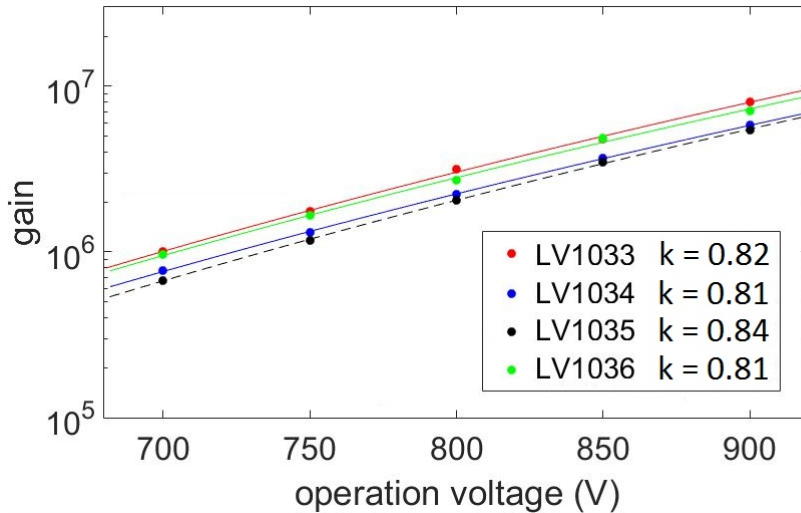


Figure 3.13: The fit function describes very well the gain measurements. The k values for these four PMTs are given in the legend.

Table 3.2: HV that has to be applied to the different PMT in order to get a gain of $2 \cdot 10^6$

PMT nr.	Voltage [V]	PMT nr.	Voltage [V]
LV1032	770.5	LV1068	751.9
LV1033	760.8	LV1070	764.3
LV1034	788.9	LV1074	810.1
LV1035	797.7	LV1075	747.3
LV1036	767.4	LV1076	801.7
LV1037	755.6	LV1079	795.7
LV1038		LV1080	767.1
LV1040	724.1	LV1153	717.9
LV1041	717.5	LV1154	745.2
LV1042	717.0	LV1155	783.2
LV1046	732.5	LV1163	724.5
LV1067	778.9	ZA2352	852.1

Chapter 4

Semiconductor Photosensors

4.1 General Description

The TPC project will not only make use of 1-inch PMTs but also of silicon photomultipliers such as APD and MPPC (Figure 4.1). Study of the behaviour of MPPCs operated in the ultra-violet light (UV-light) regime and in liquid xenon is a new research field. The characterization of a new MPPC (model: s10362-33-050) was part of this thesis. MPPCs have lower gain output signals than the PMT, hence the whole set-up for the read out has to be studied and optimized. In order to provide a better understanding of the test results, this chapter gives an introduction on APDs and MPPCs taking as primary reference the Hamamatsu Opto-semiconductor handbook [70].

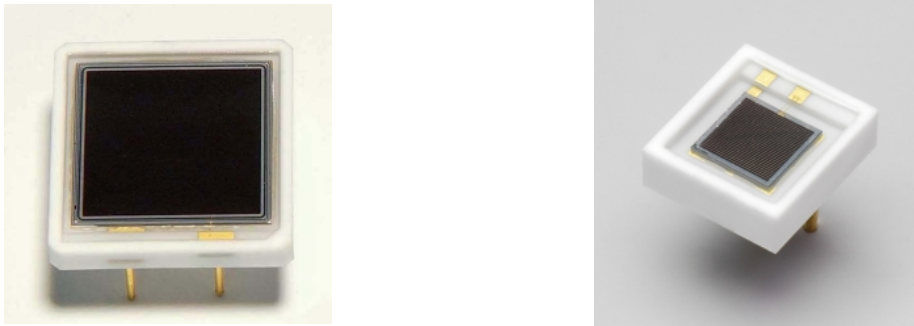


Figure 4.1: Photograph of a $12 \times 12 \text{ mm}^2$ APD (left) and a $3 \times 3 \text{ mm}^2$ MPPC (right).

4.1.1 From Semiconductors to Diodes

Semiconducting materials have properties midway between conductors and insulators. For this reason they are widely used in electronic components such as diodes and transistors. The conductivity can be controlled by current or voltage applied to a control electrode, by the temperature or, as it is the case for photosensors, by the intensity of irradiation. Common semiconducting materials are silicon (Si) and germanium (Ge). Their conductivity can be customized by implanting impurities. Semiconductors where pentavalent atoms (5 valence electrons such as phosphorus and arsenic) or trivalent ones (3 valence electrons such as boron and aluminium) have been implanted are called respectively n (negative)- and p (positive)-type semiconductors. The former present a higher number of weakly bound electrons that can easily be moved in the conducting band. On the other hand, p-type semiconductors have a deficit in valence electrons, called *holes*. When this two different semiconductor types are in contact, a so-called *p-n junction* is formed. Through this, a difference in electrical potential is created as shown in figure 4.2. The contact region between n- and p-layer, where all the charge carriers have been diffused away, is called *depletion layer*. The

n-layer site of this region becomes positively charged and the p-layer site negatively charged. This charge distribution gives rise to an electric field over the depletion layer. When a electron/hole pair is produced in the n-layer, the electron will again diffuse into the depletion region, whereas the holes drift towards the p-layer due to the electric field. Same happens to new charge carriers produced in the p-layer by inverting the electron and hole behaviour. This process goes on until the electric field becomes high enough to avoid charge diffusion, a condition of equilibrium is than obtained.

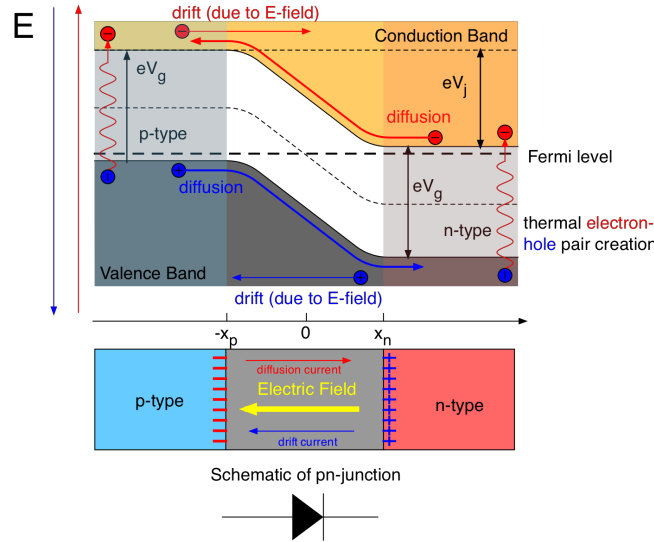


Figure 4.2: Energy band diagram for a p-n junction. Figure from [71].

Current-Voltage Relationship

A diode is a p-n junction on which the current flow can be facilitated or suppressed by applying an external electric potential. A diode is *forward-biased* when the p-layer is connected to the positive terminal and the n-layer to the negative one. This allows to the accumulated drifted charges to leave the diode weakening so the electric field in the depleting region. By increasing the supply voltage the electric resistance in the depleting region is reduced, allowing a higher current flow. This relation is represented in figure 4.3. When the electric potential is applied in the opposite direction, the diode is *reverse biased*. When operated in this way the electric field gains in strength. Therefore, only a small negative leakage current (a few nA) will flow through the junction. The electric field increases together with the applied reverse voltage until it reaches a critical level at which it breaks down and current starts to flow. The breakdown is a non-destructive processes and is reversible, as long as the amount of current flowing does not reach levels that cause the semiconductor material to overheat causing thermal damages. As described in the next section, diodes operated in the breakdown region are very sensitive to system perturbations, which can induce a significant current flow.

4.1.2 Avalanche Photodiodes

Diode in which electron/hole pairs can be produced by means of photoelectric effect are called *photodiodes*. These can be operated in different modes such as Geiger, photoconductive and photovoltaic, depending on the operation voltage. Avalanche photodiodes (APD) are optimised to be operated at high reverse bias. They are operated in the Geiger mode when the operation voltage is higher than the breakdown voltage. The photo-current generation mechanism of the APD is the same as that of a normal photodiode. When light enters a photodiode, electron/hole pairs are generated when the deposited energy is higher than the band gap energy. The ratio between

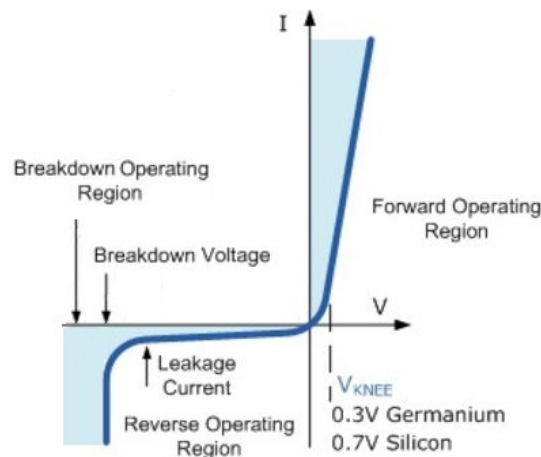


Figure 4.3: Representation of the current-voltage relationship of a diode. The diode is operated in the forward or reverse bias region depending if the applied voltage is positive respectively negative. At higher negative voltage the diode reach the breakdown operation region. Figure from [72].

the generated electron/hole pairs number related to the one of incident photons is defined as the quantum efficiency (QE). When electron/hole pairs are generated in the depletion layer they are accelerated through the electric field to the n-layer respectively to the p-layers. The drift speed of the carriers is related to the strength of the electric field. Increasing their speed, strengthening the reverse voltage, they will start to hit against the crystal lattice. Increasing it even further, over the breakdown voltage, they gain enough energy to ionize the hit atoms producing new electron/hole pairs. These are also accelerated and will ionize more and more atoms starting an *avalanche multiplication effect*. In the next section the quenching technique is presented as an avalanche multiplication stopping method. APDs have high-speed, high-sensitivity photodiode allowing large output signal current, even when detecting a single photon [73]. They require special care and handling since in the operation region small changes in the supplied voltage results in high current variations. The provided signal is described in section 4.1.3.

Quenching Resistor Technique

If an avalanche multiplication process starts it will last as long as the operation voltage is maintained. The process has to be stopped and the initial condition restored before the APD is ready for the next photon detection. This can be done by an external circuit lowering the voltage. An effective solution is to connect a resistor in series with the APD (figure 4.4), the so-called *quenching resistor* technique. The stopping voltage reduction is produced by the current, of the avalanche multiplication itself, flowing through the resistor. In a few 10 ns the APD is restored and ready for the next photon.

4.1.3 Multi-Pixel Photon Counter

Multi-Pixel Photon Counter (MPPC) consists of APDs joined in parallel as schematically represented in figure 4.4. These “APD pixel” can measure just a few 10 μm . As such, MPPCs are suitable for photon counting purposes since they offer an excellent time resolution and a multiplication function providing high gain and low noise.

MPPC Gain

For the MPPC as for the 1-inch PMT (section 3.1) the gain is defined as the charge (Q) that is read out, divided by the charge of the electron (q) produced from the incoming light. The gain,

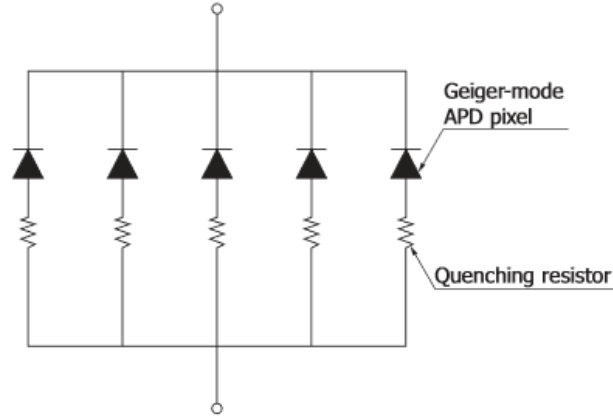


Figure 4.4: Structure of an MPPC. MPPC consists of multiple APD pixels connected in parallel. Each APD pixel has its associated quenching resistor. Figure from [70].

also called multiplication factor μ is obtained as follows:

$$\mu = \frac{Q}{q}. \quad (4.1)$$

The charge Q is the resulting charge produced in the avalanche process. This is related to the difference between the applied reverse operation voltage V_R and the breakdown voltage V_{BR} ($V_R > V_{BR}$ in Geiger mode). The resulting charge Q is given in equation 4.2, where the C is the capacitance of one pixel:

$$Q = C (V_R - V_{BR}). \quad (4.2)$$

From equations 4.1 and 4.2 it appears that the gain has a linear dependency with the operation voltage. Operated in Geiger mode the device provides a gain of about 10^5 to 10^6 . The MPPC is a very temperature sensitive device. Increasing the temperature the crystal lattice vibration becomes stronger increasing the probability of a charge carrier to hit the lattice before it becomes energetic enough to start an avalanche. Lowering the temperature lowers also the V_{BR} .

Dark Count

Dark counts denote all the signals that are measured but have not been generated from a photon hitting a pixel, produced instead by thermally generated carriers. The pulses produced from the thermally generated carriers are called dark peaks, and these are not distinguishable by the shape from a photoelectron generated peak. Hamamatsu defines as *dark pulse* pulses having at least half the height of a single photoelectron peak (0.5 p.e.), but not originated from a photon [70]. The dark count rate is a parameter that gives the number of dark pulses per second. Since this pulses are generated by thermal produced carriers, the dark count rate $N_{0.5p.e.}$ presents a strong temperature dependency. The rate temperature T (Kelvin) dependency is given as:

$$N_{0.5p.e.}(T) \approx AT^{\frac{3}{2}} \exp \left[\frac{E_g}{2kT} \right], \quad (4.3)$$

where A is an arbitrary constant, E_g is the band gap energy (eV) and k the Boltzmann's constant. The dark count rate is strongly suppressed lowering the temperature. Hamamatsu tested a MPPC with similar characteristics of the ones that have been tested as part of this thesis, and has obtained a 90% lower rate by a temperature reduction of 27 K.

MPPC Signal

In a MPPC each of its pixels, when hit by a photon, produces the same current pulse signal. If a number of pixels n detect a photon at the same time, then the outcoming current will be $\times n$ that produced by a single photo detection. An example can be seen in figure 4.5. As discussed in the previous section, each pixel after detecting a photon has to be restored, and if multiple photons hit the same pixel their information get lost. The linearity of the outcoming signal related to the incoming photons gets worsen by increasing the irradiation intensity.

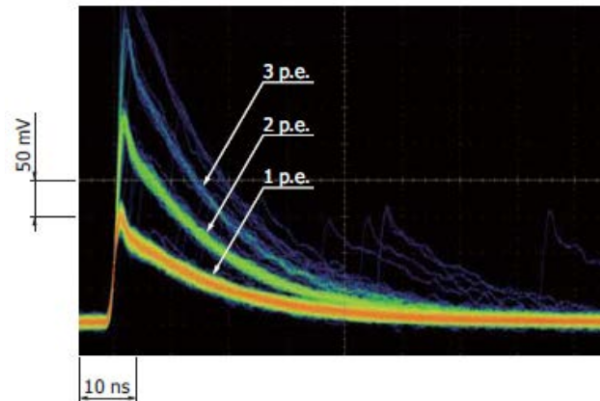


Figure 4.5: Pulse waveforms for single and multiple photon detections. MPPC signals rise in a few ns and decrease in a few 10 ns. Figure from [70].

4.1.4 $3 \times 3 \text{ mm}^2$ MPPC Models

Different models of MPPCs from Hamamatsu Photonics have been tested, but all of them have some common features. They have an active surface of $3 \times 3 \text{ mm}^2$, no protecting window, in order to increase the photon detection efficiency, and are installed on a ceramic package. These MPPC models have 3600 pixels with a $50 \times 50 \mu\text{m}$ area. The following models have been used:

- 33-050-UVE-NO-WINDOW, Serial No. 1
- S12754-050C, Serial No. 3 and No. 4
- 3x3 MM-50UM VUV2, Serial No. A0007 and No. A0009

In order to distinguish the different MPPCs, from now on the serial number will be used. The A0007 and A0009 are the newest model that Hamamatsu provided for the tests.

4.2 Experimental Set-up

4.2.1 General Set-up Requirements

MPPCs have a lower gain than the 1-inch PMT, and the signal peak is about ten times shorter. The requirement of a low noise set-up and stable electronics is essential, as well as a good time and energy resolution in order to be able to separate the signal produced by N -photon from the one produced by $(N+1)$ -photon (N stands for the number of detected photons). In figure 4.2.1 an ideal photoelectron spectrum is represented.

As for the 1-inch PMT a light-tight environment is needed. At the beginning of my work (12.2014) Julian Wulf was testing the MPPC in the MarmotXL (section 2.3.2). The first tests performed for this thesis were made in the BB described in section 3.3.1, in which the first useful data were obtained, and in the last months spent in the laboratory the Liquid Argon Set-up was prepared (section 4.2.2).

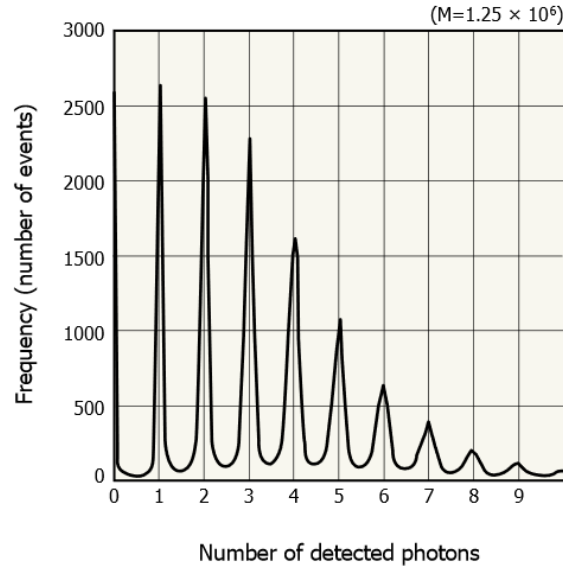


Figure 4.6: Ideal photoelectron spectrum at low light where the N -photoelectron peaks are clearly distinguishable and their frequency decrease is described by a Gaussian distribution with the mean value at one photon detected at the time. An increase of the light would move the mean value of the distribution to the right. Figure from [70].

4.2.2 Liquid Argon Set-up

The Liquid Argon Set-up (LArS) has been built at the University of Zurich and used for performing complex and very accurate measurements on components that had to be installed in GERDA [74]. Smaller than MarmotXL and designed for argon liquefaction, LArS presents a proper set-up to test the MPPC at different temperatures. The LArS has been adapted for the MPPC tests by increasing the number of feedthroughs in order to be able to operate up to four PDs at the same time. Connectors for the two thermometers, LED and heater resistor have been implemented (figure 4.7). For this set-up, in order to reduce the pick-up noise, new double shielded cables have been used for all connections needed to read out the signal.

Cooling System

The tests were performed in vacuum, and the cooling power was provided by liquid nitrogen flowing through a copper coil (figure 4.7 right). The temperature is set by changing the flow rate of the nitrogen. The lowest temperature that can be reached is around 77 K, but tests have never been performed at temperature lower than 150 K. The high pressure nitrogen flow, coming from a 1501 dewar, is regulated with a valve (Cooling Power Control Unit) located at the end of the copper pipe (outside the LArS). To stabilize the temperature inside the chamber, a heater, connected to the copper coil and controlled with an external cryogenic temperature controller (Cryocon 32), was implemented. This vital component allows to run the experiment also in absence of direct supervision. In order to reach a stable set-point, the cooling and heating powers must be balanced. It has been seen that the heater should be set at around 20% of its power in order to have good stability. The temperature can be controlled very precisely (<0.1 K) inside the chamber.

Slow Control System

The LArS is supported by a Slow Control System (SCS) (slow: its sampling rate is below the Hz range). The SCS has two main tasks: the monitoring and control of the conditions, and the safety management. Concerning the former, it has been used for the constant verification of pressure,

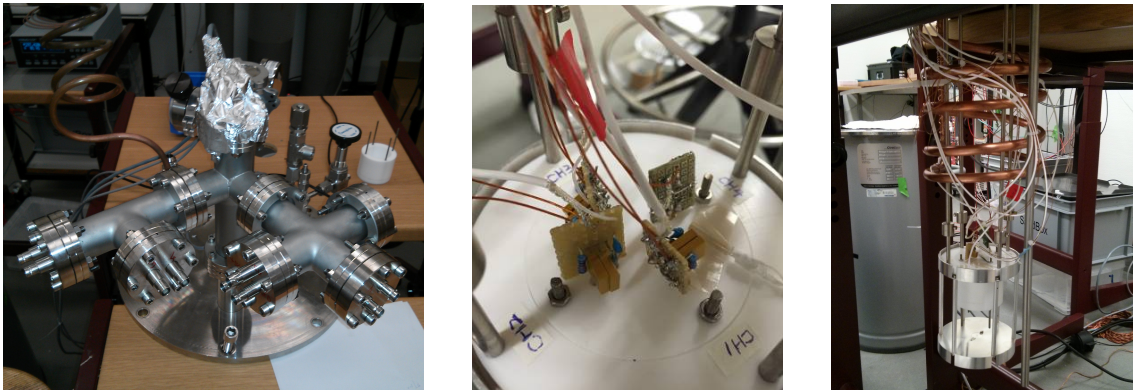


Figure 4.7: (left) Photograph of the top part of the LArS where all feedthroughs for signal, HV, LED, heater and temperature sensor are placed. (middle) Top disk of the holder with the MPPCs installed, the bases and cabling can be seen. (right) Photograph of the inner part of LArS. Visible is the cooling copper coil, the cabling going to the four MPPCs and at the bottom the PTFE holder.

temperature and high voltages. Furthermore, two webcams connected to the SCS show the status of the dewar and the cooling power control unit. All data are recorded and can be displayed as function of time. The supply voltage, provided to the tested MPPCs, can be controlled remotely. The safety mode reacts when a parameter exceeds the set operation range sending an alert signal via mail and SMS to the people working on the project.

MPPC Holder

The MPPCs are kept in place with a PTFE holder shown in figure 4.7 (middle). The main part of the holder, excluding the top disk (see figure 4.7 middle), is designed to host a temperature sensor and an LED. The top disk is an interchangeable element that can be substituted when MPPCs with different size have to be tested. Given the small size of the $3 \times 3 \text{ mm}^2$ PDs it was possible to test four of them at the same time. The holder is fixed by an aluminium case just below the cooling coil.

4.2.3 Electronic Equipment

The electronic set-up is similar to the one presented in section 3.3.2 and figure 3.4. During the first test a picoammeter and a power supply, with a stability down to nV, were used in order to have very stable and precise supply voltage. The picoammeter provides an accurate current measurement. During the test in the BB the signal was not triggered with the pulse generator but through a discriminator.

Amplifier

The test was performed using different amplifiers. The Philips model 744 has sixteen channels and a fixed amplification factor of ten, whereas the model 777 has eight settable channels, and the amplification factor can be varied between 2 and 50. For the test with the LArS, also a $\times 10$ amplifier built at the electronic workshop at the University of Zurich was used. Some tests have been performed using a pre-amplified base, this could provide amplification up to factor 1000.

MPPC Base

To build a suitable base for the MPPC was part of this thesis. The basic connection diagram is represented in figure 4.8 (left). The base has to be as light as possible in order to not bend

the MPPC socket under its weight. The high resistor ($10\text{ k}\Omega$) at the anode, together with the grounded $0.1\ \mu\text{F}$ capacitor, are used as a low pass filter that prevents pick-up noise from possible supply voltage oscillations. The $50\ \Omega$ grounded resistor together with the $0.1\ \mu\text{F}$ capacitor transform the produced current signal into a voltage, which is then read out and digitized. This electronic component also filters out all the long signals that can rise from some constant noise. One pole of the supply voltage and signal are grounded.

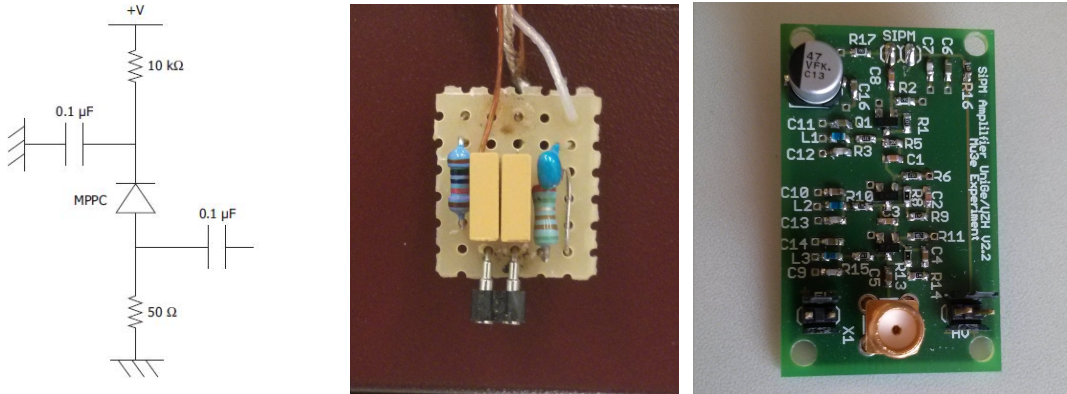


Figure 4.8: (left) The connection diagram of the MPPC bases. This base transforms the produced charge current into a voltage signal. (middle) Photograph of a base that has been built and used for data taking already connected to the power supply and signal cables. (right) Photograph of the base used for silicon photomultipliers in Mu3e experiment [75], that is provided with a pre-amplifier, but the base concept follows the connection diagram on the left.

4.3 MPPC Gain Measurement

The data acquisition and the processing are as for the 1-inch PMT and are explained in sections 3.3.3 and 3.3.3. During the test at room temperature the dark count rate was high enough to provide useful waveforms without using the LED as light source.

4.3.1 Gain Calculation

After the data have been processed following the procedure described in section 3.3.3, the gain is obtained from the position of the different photoelectron peaks. In figure 4.9 one of these processed spectra and the fit on the data are shown. The fitting function is obtained adding five Gaussians and is given in equation 4.4. For the different Gaussians the values of the expectation values (μ), the width (σ) and amplitudes (a) are given as free parameters, the only initial parameters required by the fitting program are the regions in which the different peaks are located:

$$f(x) = \sum_{i=1}^{n=5} a_i \cdot \text{Gauss}(\mu_i, \sigma_i). \quad (4.4)$$

The gain can then be calculated knowing that the difference between two peaks that follow each other is related to the detection of one more photon. The ADC counts are defined as in section 3.3.3, and one single channel corresponds to $1.71429 \cdot 10^5$ elementary charges. The number of ADC channels between two peaks gives the number of detected electrons that corresponds to the one produced from a single photon event. Dividing the charge difference between two peaks by the elementary charge the gain is obtained. In order to reduce the error arising from the fitting

function, the difference between the first three signal peaks could be used as given in the following equation:

$$gain = \left(\frac{(\mu_2 - \mu_1) + (\mu_3 - \mu_2)}{2} \right) \cdot 1.71429 \cdot 10^5. \quad (4.5)$$

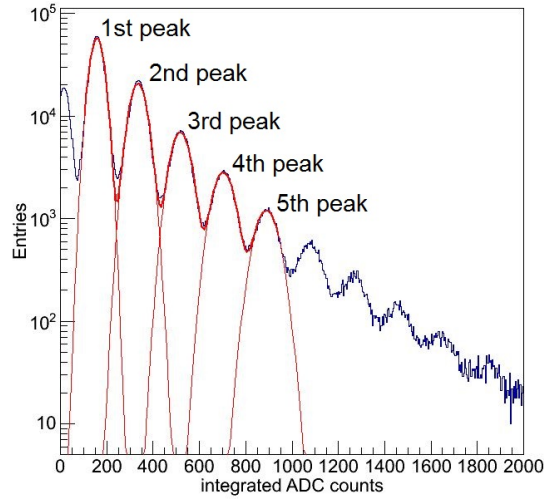


Figure 4.9: Spectrum, in semilogarithmic scale, obtained after processing the collected data. The peaks from the left are one noise peak followed by the single, the double, the triple, ect. photoelectron peaks. Five Gaussians have been fitted to the first five photoelectron peaks (labeled).

4.3.2 First Test in MarmotXL

At the beginning of my work on MPPCs described in this thesis, the silicon detectors A0007 and A0009 were installed in MarmotXL (figure 4.10) and cooled down to 172 K. With the set-up that was already prepared only spectra with no distinguishable signals peaks have been obtained. The reason why no photoelectron peaks are observed has been attributed to an unstable operation voltage. The used power supply (CAEN) has an error in the Geiger mode operation region (around 60-64V) of about ± 2 V. But oscillations in the operation voltage of a few 10 mV makes the gain measurement impossible.

In order to determine the breakdown voltage V_{BR} , used to define the most appropriate reverse voltage V_R , the current dependency of the supply voltage for the two MPPCs was measured with high precision (pA and nV). The data collected are represented in figure 4.11. These measurements have been performed using the electronic components described in section 4.2.3.

4.3.3 Black Box

In order to reduce the background signal the BB has been moved to another laboratory presenting less electromagnetic noise. Also in the new location no signal was observed, so contact has been taken with Roman Gredig. He is a member of the group of Prof. Ulrich Straumann and is working with MPPCs since a few years. Thanks to his advice and the pre-amplifier base he lent me (figure 4.8 right) the first gain measurement has been performed. Thanks to the data collected with the pre-amplified base the proper operating voltage has been found. Knowing the operational voltage and using an external amplifier data were also obtained with the base shown in figure 4.8 (middle). The first hint of a signal has been obtained using the $\times 10$ amplifier, and the first useful data have been collected using an amplification factor of fifty (figure 4.12).

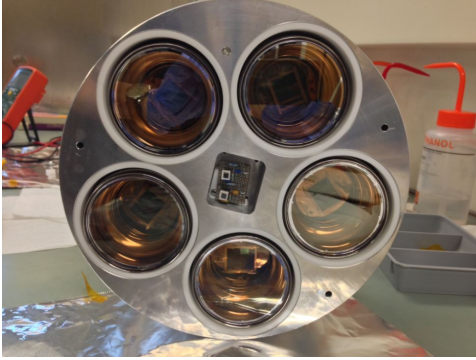


Figure 4.10: Photograph of the bottom of the aluminium filler with five 3-inch PMTs and two MPPCs installed. The filler is placed in the inner chamber of MarmotXL, where the xenon is liquefied.

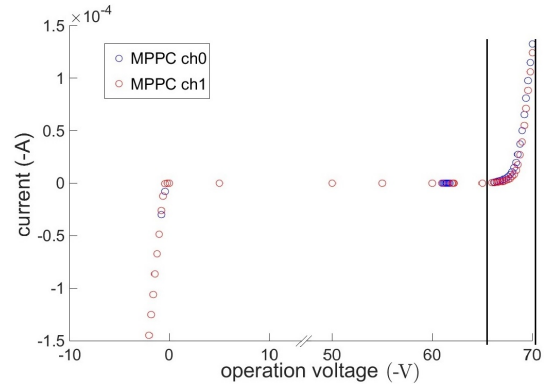


Figure 4.11: Measured current as a function of the supply voltage for the MPPCs A0007 and A0009 at 172 K. The region between -10 V and -60 V is not represented since the current value is constant zero. The operation region is demarcated by the two black vertical lines. Higher negative voltage has been avoided in order to not damage the MPPCs.

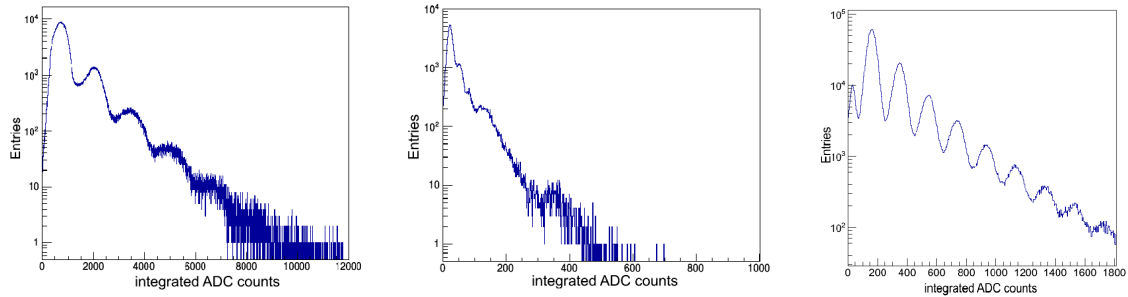


Figure 4.12: Spectra obtained after processing the data collected using different amplifiers. The base with the pre-amplifier has an amplification factor that depends on the voltage provided to it (left). Using the Philips $\times 10$ amplifier model 744 the first peak structure was observed using the new base (middle), but only using the Philips $\times 50$ amplifier model 777 a very nice spectrum has been obtained (right).

4.3.4 LArS

Next step in MPPC testing is to study the gain behaviour at different temperatures. In the LArS set-up, four $3 \times 3 \text{ mm}^2$ MPPC can be operated at the same time, so the newest model and the best working of the older MPPC have been installed (A0007, A0009, No.3, No.4). For the first three MPPCs the new base was used and for the fourth the one in loan. Once the MPPCs have been installed inside the vessel, it has been evacuated to a pressure of 0.02 mbar. The pressure reduction is not done to carry out tests in vacuum, but to prevent that the air humidity freezes during the cool-down, damaging the PDs. Small variation on the power supply of the Philips amplifier produced a smearing out of the peaks, making it impossible to distinguish the individual photoelectron peaks. The problem was solved using the amplifier produced by the University of Zurich electronic shop which was powered by another much more stable source. Due to the low background light and strong suppression of the thermally produced signals, for the measurements at low temperature, an LED had to be used as a light source. For a clear signal detection, thanks to the low electronic noise of the set-up, the $\times 10$ amplification was already enough. Since the power-supply for the pre-amplified base used for the MPPC No. A0009 produced a lot of noise in all the channels, it was decided to use only the three stable channels.

4.4 Results and conclusions

4.4.1 Gain at Room Temperature

In figure 4.13 the gains obtained from the measurements at room temperature using the BB are represented and the corresponding measured currents are shown in figure 4.14. As expected from calculation performed in section 4.1.3 the gain is linear in operation voltage.

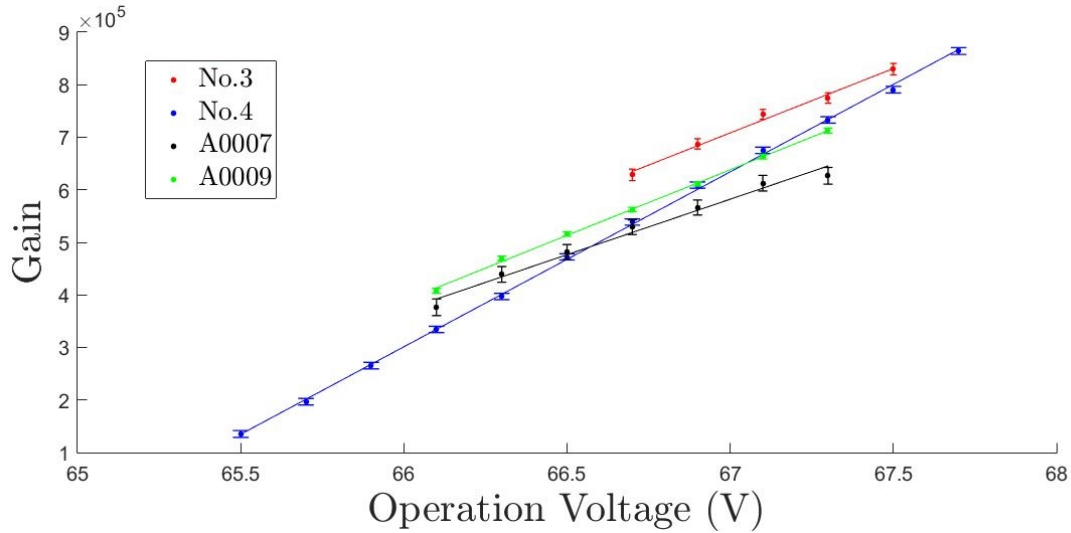


Figure 4.13: Collection of the gain measurements performed at different voltages at room temperature and pressure. Results for MPPC No.1 are not shown since its operating voltage is above 70 V. The chi2 errors obtained by fitting a linear function on the data are smaller than 1 %.

For the gain measurement, the information obtained from the first three signal peaks was used as given in equation 4.5. Only later on, working at the optimisation of the fitting function, it has been noticed that the peaks were not exactly equidistant as supposed initially. This phenomenon has been analysed (figure 4.15) and attributed to after-pulse events. These events are produced by carriers generated during the avalanche multiplication process that are trapped by lattice defects. If they subsequently escape the trap, they produce a new signal that is not distinguishable from an original photoelectron signal. If an after-pulse is produced within the same range of the initial signal, the processing program will add both areas. This would result in a shift of the peak in the spectrum to the right and makes resulting gain 14% and 18% higher at an operation voltage of 66.6 V and 67.5 V, respectively.

4.4.2 Conclusions and Outlook

The knowledge required to characterize MPPCs has been acquired. The main requirement is a very low electronic noise background environment and stable electronic components, for example, double shielded cables and stable power supply. MPPCs provide narrow peaks signals up to quadruple photoelectron events detected at room as well as low temperature (down to 110 K). As described in Chapter 4.1.3, the gain has a strong temperature dependence, this has been studied by J. Wulf and the results are shown in figure 4.16. New MPPC models with larger active areas will be tested in order to identify the most suitable candidate for the TPC.

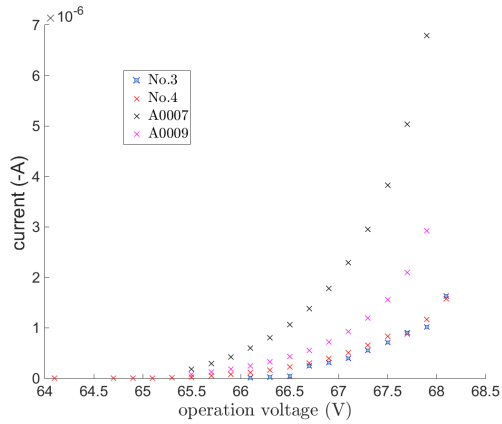


Figure 4.14: Representation of the current as a function of the supply voltage in the operation region.

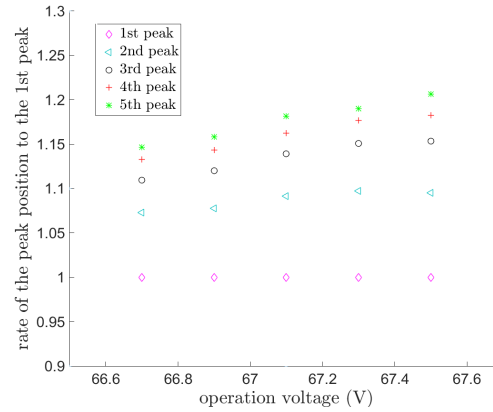


Figure 4.15: Higher order signal peak position divided by their order related to the SPE peak for the MPPCs tested. At higher supply voltages the shift increases. On the other hand, the displacement between the higher orders seems to be constant.

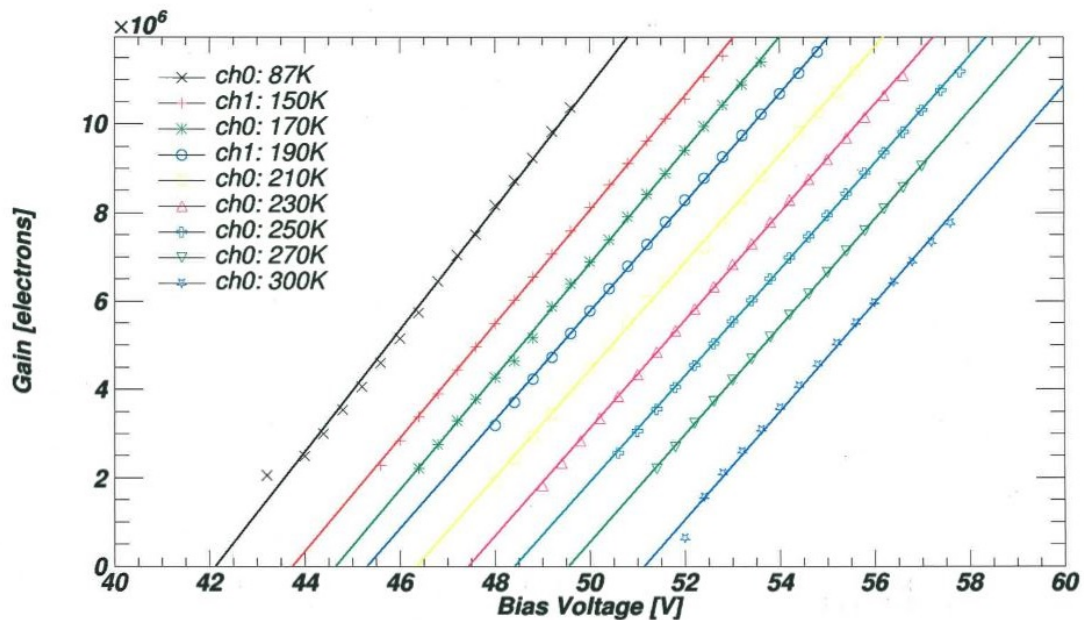


Figure 4.16: Collection of gain measurements as a function of the operation voltage at different temperatures for MPPC No. 3. A strong linearity can be observed as well as the fact that reducing the temperature at a given operation voltage the gain increases.

Chapter 5

Design and Monte Carlo simulation of a Time-Projection Chamber

The light collection efficiency (LCE) of a TPC can be influenced by the configuration of the PD arrangement and by the geometry of the TPC. In this thesis the best solution for the top array has been investigated in order to obtain a high LCE and homogeneity. The latter is a requisite for a precise position reconstruction. All the studies have been performed through Monte Carlo simulations (section 5.1.3). Once the optimal PD configuration has been found, further small changes have also been analysed and are discussed in the conclusions.

Using Geant4, different arrangements of the PDs have been simulated in order to find out the best array arrangement for a given number of PDs. Furthermore, the geometry of the chamber itself has been adapted in order to obtain the highest LCE and a good homogeneity.

5.1 Monte Carlo Simulations

For the studies of the LCE for S1 and S2 the inner region of the TPC has been simulated. This involves the bottom and top photodetector arrays, the xenon in liquid (LXe) and gas (GXe) phases as well as the geometry of the vessel. For these studies no electric field had to be implemented, and the results provided are purely used for the geometry optimisation and return no information about the overall detector efficiency.

5.1.1 TPC Geometry

The size limitations of the TPC are given by the MarmotXL inner chamber that will host the TPC (section 2.3.2). All the inner surfaces of the TPC are made of PTFE due to its high degree of reflectance (section 5.1.2) at the wavelength of the produced photons. Most of the geometry of the TPC is shown in figure 5.1 and consists of a top and a bottom plates (diameter 236 mm), the side wall in the LXe region and an element for adapting the width of the bottom part to the top one. At the beginning the volume of the LXe was supposed to be a right prism with a decagon base with ten independent wall sections. This was the same method used in XENON100 to prevent deformation of the inner volume due to PTFE thermal contraction. Due to the smaller size of this TPC, the thermal contraction would produce very small deformation and since it is possible to machine a PTFE tube of the same radius of the TPC, hence a cylindrical volume has prevailed. The inner radius has been chosen to be 10 cm, corresponding to the central position of the outer circle of PMTs (figure 5.2). The distance between the top and bottom plates and between the top plate and the liquid surface had to be optimized through Monte Carlo (MC) simulation, taking

into account that the maximum height inside the TPC is 140 mm. The LXe target volume for optimized geometry corresponds to 2.4 dm^3 and a mass of 7.8 kg ($\rho = 2.9 \text{ g/cm}^3$).

5.1.2 Material Properties

The choice of the material in contact with the target volume plays an important role. The xenon, with characteristics discussed in Chapter 2, is in contact with the PDs and the wall of the TPC chamber. The PMT windows are made of quartz that has a high transparency to wavelength of the xenon scintillation, whereas the MPPCs have no protection window. The rest of the chamber is entirely made of PTFE. This choice is supported by its properties listed below.

PTFE

The chemical name of the well-known Teflon is polytetrafluoroethylene (PTFE). PTFE has many desirable properties, because it is hydrophobic, non-reactive, chemically inert, has a high melting point and excellent dielectric properties [76, 77]. The strong bond between carbon and fluorine leads to a high chemical stability in a wide range of temperatures between $-200 \text{ }^\circ\text{C}$ and $260 \text{ }^\circ\text{C}$, which makes it suitable for use in xenon scintillation detectors. Teflon is widely used in construction of TPCs, both as electrical insulator and as a light reflector to improve the efficiency of detection of scintillation photons. In the wavelength region between 250 and 2500 nm PTFE presents a very high reflectivity (up to $\sim 98\%$) [78, 79]. On the other hand, in the vacuum ultraviolet wavelength region ($\lambda=175 \text{ nm}$), corresponding to the xenon emission light, the reflectance distribution function needs to be further investigated [80]. Precise knowledge of the material properties will improve the simulation results.

5.1.3 Software Support

Monte Carlo Methods

The core idea of a Monte Carlo (MC) simulation is to use random samples of parameters or inputs to explore the behaviour of a complex system or process. These simulations are mainly used for optimization, numerical integration, and probability distribution analysis. In experimental particle physics, MC methods permit to understand the behaviour of the detectors, compare experimental data to theory and background modeling. The Monte Carlo simulations of the TPC have been performed with the Geant4 (version Name: geant4-09-06-patch-02) toolkits developed for the simulation of particles passing through matter [81]. It is provided with physics lists that implement physical effects such as scintillation, refraction, reflection, absorption and Rayleigh scattering to name a few.

5.1.4 Simulation Parameter

The LCE was obtained by generating 300'000 events isotropically generated, each of them consisting of a point source emitting 3'000 VUV-photons with an energy of 6.98 eV uniformly distributed over 4π . This energy corresponds to a wavelength of 178 nm that is the one of the scintillation light emitted in S1 and S2. For the LCE in S1, the events have been uniformly distributed in the LXe volume, instead the S2 events are generated within a thin disk in the gas phase, $(1.0 \pm 0.5) \text{ mm}$ above the liquid-gas interface, where electro-luminescence takes place. The random function used was G4UniformRand() which returns an uniformly distributed value between zero and one. Through this simulation the LCE is obtained for every event. Figure 5.1 represents one event of 100 photons for the LCE in S1 (left) and in S2 (right).

5.1.5 Bottom and Top Arrays

The bottom array is constituted by 3-inch PMT and one 1-inch PMT. For the second array up to three different PD types are used together: 1-inch PMT, APD and MPPC. The model and number

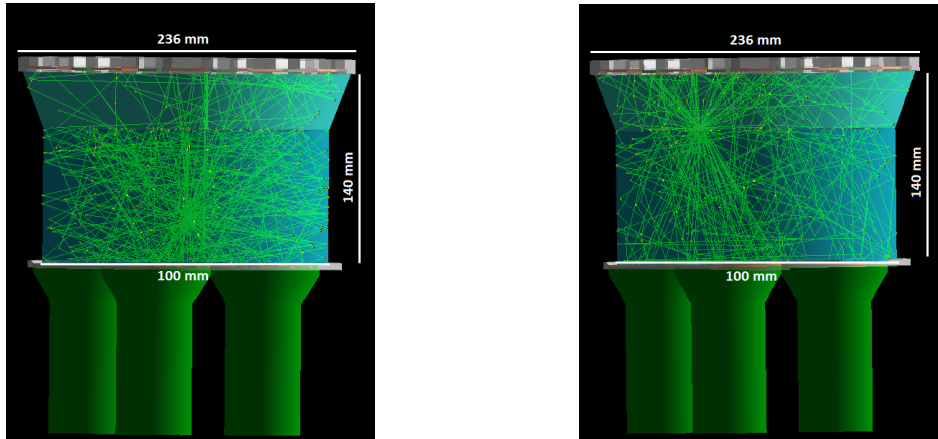


Figure 5.1: Graphic representation of the simulation of one event with 100 photons for an S1 signal (left) and an S2 signal (right). The PTFE wall had been set as invisible in order to give a view of the interior of the TPC. The number of photons has been reduced to 100 in order to be able to distinguish the tracks of the photons. Most of the S1 photons are detected by the bottom PDs since a large fraction of them reflects on the liquid-gas surface. The bottom array is constituted of five 3-inch PMTs and one 1-inch PMT, the top array of 1-inch PMT, APD and MPPC.

of MPPCs that will be purchased will be decided once the knowledge of their behaviour is acquired. These two factors have been taken into consideration testing also configurations including different numbers of MPPCs and changing their size (3×3 , 6×6 , $12 \times 12 \text{ mm}^2$). Most of the simulations have been performed with the following type and number of sensors;

- 21 1-inch PMTs model R8520 (described in Chapter 3)
- 12 APDs (model: s1315 $14 \times 14 \text{ mm}^2$)
- 0-16 MPPCs $3 \times 3 \text{ mm}^2$ (described in Chapter 4)
- 5 3-inch PMTs (model: R11410-20)

Figure 5.2 shows the first top array design realized with SolidWorks (see section 5.2).

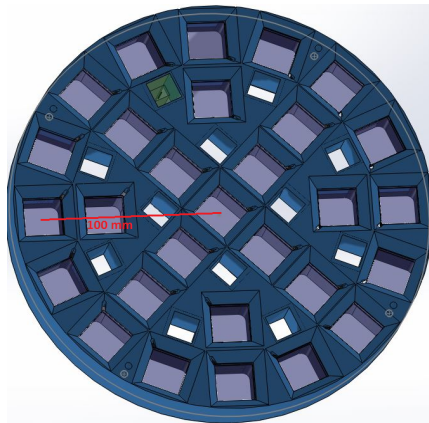


Figure 5.2: First drawing in SolidWorks of the top array holder where no MPPC was considered, only the 21 PMTs and the 12 APDs. The top plate radius is of 118 mm and the circle on which the outer 1-inch PMT are centred has a radius of 100 mm. Simulations have been performed where sloped PMT hole shapes have been considered.

5.1.6 Code Evolution

1st Step

Starting from a Xenon based example supplied in the tutorial of Geant4, the geometry and the properties of the materials have been adapted in order to correspond to those of the TPC. The physics lists describing the general physical properties, the standard electromagnetic interactions, and the optical physics have been implemented. The result of the simulation depends significantly on the optical parameters of the different used materials. The most influential optical parameters are listed in table 5.1.

Table 5.1: Important optical physics list parameters for photon of 178 nm wavelength

Parameter [m]	Value
LXe Absorption length [m]	5
LXe Rayleigh scattering length [m]	0.3
LXe refractive index	1.61
GXe Absorption length [m]	100
GXe Rayleigh scattering length [m]	100
GXe refractive index	1
Photo cathode refractive index	1.56
Photo cathode absorption length [nm]	1
Quartz refractive index	1.56
Quartz absorption length [m]	30
PTFE refractive index	1.61
PTFE reflectivity	0.95
Steel reflectivity	0.2

2nd Step

The code was improved by comparing it with these used for the XENON1T and XENON100 simulations. The accurately reproduced 1-inch and 3-inch PMTs design has been taken from them, replacing the simple detector surfaces used before. This reduced the light collection efficiency due to photons being reflected on the quartz window of the PMT, instead of hitting the photocathode, but increased the reliability of the simulation.

3rd Step

Once the physics in the simulation was implemented, different runs were performed changing the geometry of the detector in order to achieve the highest and most homogeneous distribution of the LCE in S2. Once the optimised parameters for the top array were fixed, such as the distance from the liquid surface or the geometry of the holder, small changes were performed to optimise the S1 LCE.

5.1.7 Analysis of S2 Simulations

For the analysis performed in this section, the LCE percentage given refers only to the light collected by the top array. In table 5.2 the simulated top array configuration, the value of the LCE in S2 and the relative standard deviation are given. The standard deviation is used to estimate the homogeneity. The table provides also information about the changes performed in respect to the previous simulation.

For the last photodetector arrangement (Configuration 4), simulations for different distances between the LXe surface and the top array have been performed in order to study the photon distribution over the top PDs. These simulations have been named as “Simulation X”, where X refers to the number of the simulation. The photon distribution plays a crucial role in position reconstruction. When an electron is released at the interaction point, it is drifted by the strong electric field into the gas phase, where it produces an S2 signal. Since the general motion of the electron is in the z direction, the S1 and S2 signals are produced in the same place in the xy plane. If the photons produced in S2 are detected over many PDs, the position reconstruction can be very precise. For this reason the top array is provided with numerous PDs, and not just 5 3-inch PMTs like the bottom array, whose task is the detection of the small S1 signals. The results of the simulations are summarized in table 5.3. For short distances, like in Simulation 1 (1.5 cm), a higher inhomogeneity can be observed. This arises from the fact that the event position strongly influences the LCE. Events located in front of a PD will have higher LCE than the ones that are not. By increasing the distance, the produced photons are detected by a greater number of PDs, and an improved xy-position reconstruction is possible. The plots in the third column of table 5.3 show the event LCE distribution. For a good homogeneity the peak must be sharp, this would mean that most of the events have the same LCE. A compromise between signal distribution and LCE had to be found, but in general, distance changes in the order of a few millimetres had repercussions of only 1-2% in the S2 LCE.

Simulation 3 and Simulation 4 present a similar sharp peak in the LCE distribution graphs and differ only in the geometry of the chamber walls as represented in figure 5.3. In figure 5.4 the LCE as a function of r^2 is represented for different simulations performed. It can be seen that the difference between Simulation 3 and Simulation 4 is small and involves predominantly the outer region. As described in section 2.1.1, the gate is placed slightly below the liquid surface and the anode right above it. The realisation of a chamber like the one simulated in Simulation 4 (see figure 5.3 left) is to be preferred given its easier realisation.

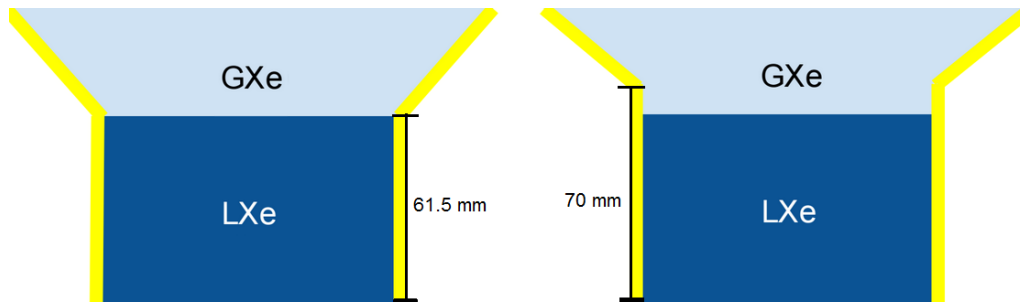


Figure 5.3: Schematic representation of the difference between Simulation 3 (left) and Simulation 4 (right). The LXe height and the distance between LXe surface and top PD array is the same, but the height at which the chamber changes its slope is different. Table 5.3 contains the geometric parameters considered for the different simulations.

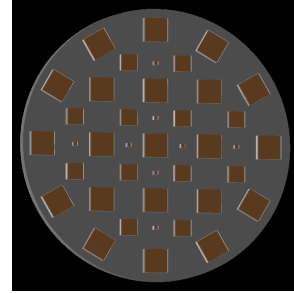
Table 5.2: Various configurations of the top PD array. The number and types of photosensors are given, together with the corresponding LCE of the top array. The reported uncertainty on the LCE corresponds to the standard deviation.

Configuration 1

Photodetectors:

- 21 1-inch PMTs
- 12 APDs
- 8 3×3 mm MPPCs

S2 LCE: $(20.0 \pm 2.1) \%$



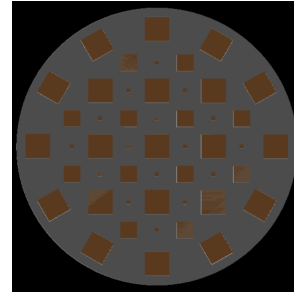
Configuration 2

The number of MPPCs was increased

Photodetectors:

- 21 1-inch PMTs
- 12 APDs
- 16 3×3 mm MPPCs

S2 LCE: $(23.5 \pm 2.0) \%$



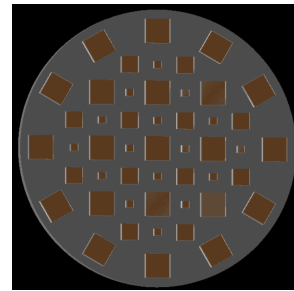
Configuration 3

The size of the MPPCs has increased and the geometry of the TPC was improved

Photodetectors:

- 21 1-inch PMTs
- 12 APDs
- 16 6×6 mm MPPCs

S2 LCE: $(24.2 \pm 1.5) \%$



Configuration 4

The number of PDs and the size of the MPPCs have been increased

Photodetectors:

- 21 1-inch PMTs
- 12 APDs
- 28 12×12 mm MPPCs

S2 LCE: $(29.5 \pm 1.5) \%$

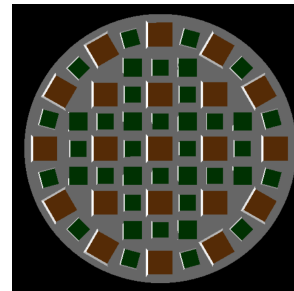
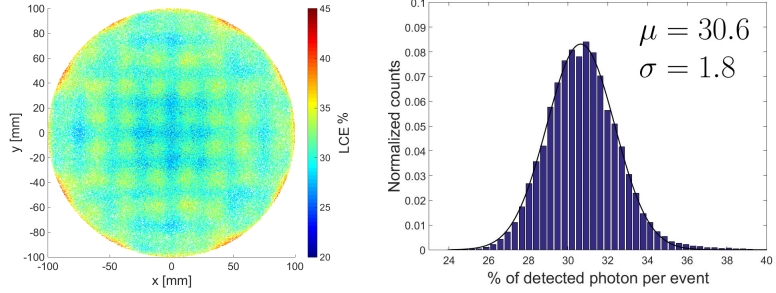


Table 5.3: Collection of the results obtained for simulations with different distances between the liquid-gas interface and the top DP array. On the left the z positions of the relevant elements are given, the S2 LCE is shown once in x-y representation and as a 1D histogram. The histograms have been normalised to the total amount of detected photons N_{tot}

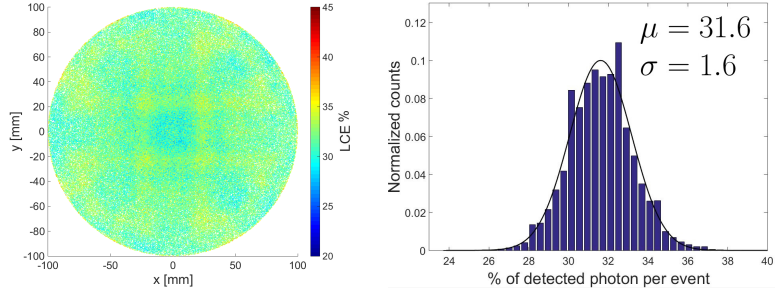
Simulation 1;

- top plate = 76.5 mm
- LXe level = 61.5 mm
- edge on the wall = 61.5 mm
- cathode = 0 mm
- bottom plate = -15 mm



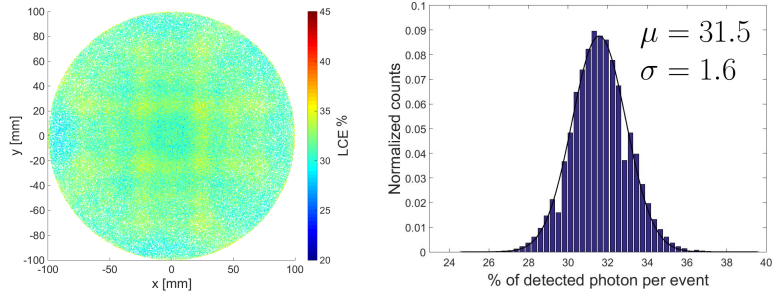
Simulation 2;

- top plate = 81.5 mm
- LXe level = 61.5 mm
- edge on the wall = 61.5 mm
- cathode = 0 mm
- bottom plate = -15 mm



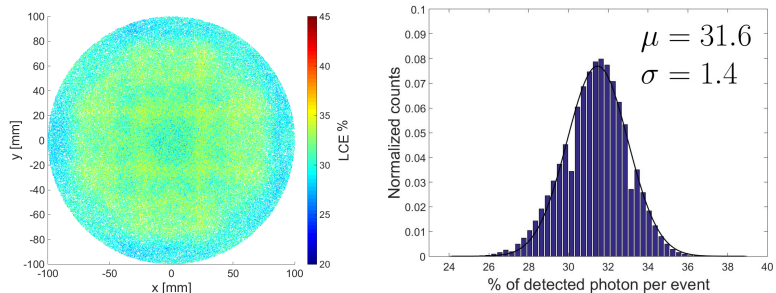
Simulation 3;

- top plate = 86.5 mm
- LXe level = 61.5 mm
- edge on the wall = 61.5 mm
- cathode = 0 mm
- bottom plate = -15 mm



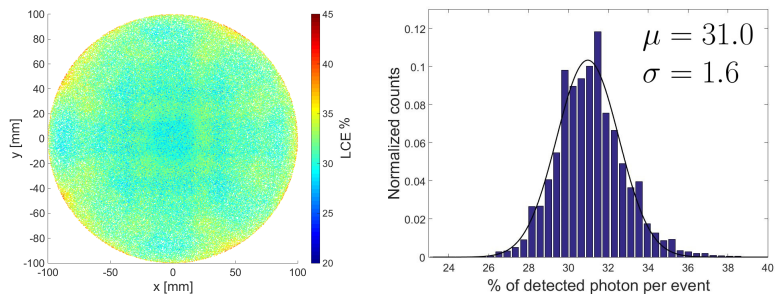
Simulation 4;

- top plate = 86.5 mm
- LXe level = 61.5 mm
- edge on the wall = 70 mm
- cathode = 0 mm
- bottom plate = -15 mm



Simulation 5;

- top plate = 86.5 mm
- LXe level = 61.5 mm
- edge on the wall = 61.5 mm
- cathode = 0 mm
- bottom plate = -15 mm



Simulation 3 and Simulation 5 differ only by their hole geometries in the top array holder: holes in Simulation 3 have a funnel shape with a slope of 45° , while in Simulation 5 the edges are sharp. The former with its 31.6% LCE for S2 and a standard deviation of 1.4%, compared to the 31.0% LCE and 1.6% standard deviation of Simulation 5, is to be preferred.

Based on Simulation 4, Simulation 6 has been performed by reducing the number of MPPCs. The design used is the same as Configuration 1 but instead of using MPPCs with a $3 \times 3 \text{ mm}^2$ active area, the ones with $12 \times 12 \text{ mm}^2$ have been implemented. The LCE S2 dropped from $(31.6 \pm 1.4)\%$ to $(26.3 \pm 1.5)\%$ for the top array, and the overall LCE from $(72.0 \pm 1.5)\%$ to $(68.8 \pm 1.5)\%$. The fact that reducing the number of PDs leads to a reduction of the LCE is not surprising, but the homogeneity shows the similar pattern as Simulation 4 as a function of r^2 , as illustrated in figure 5.4.

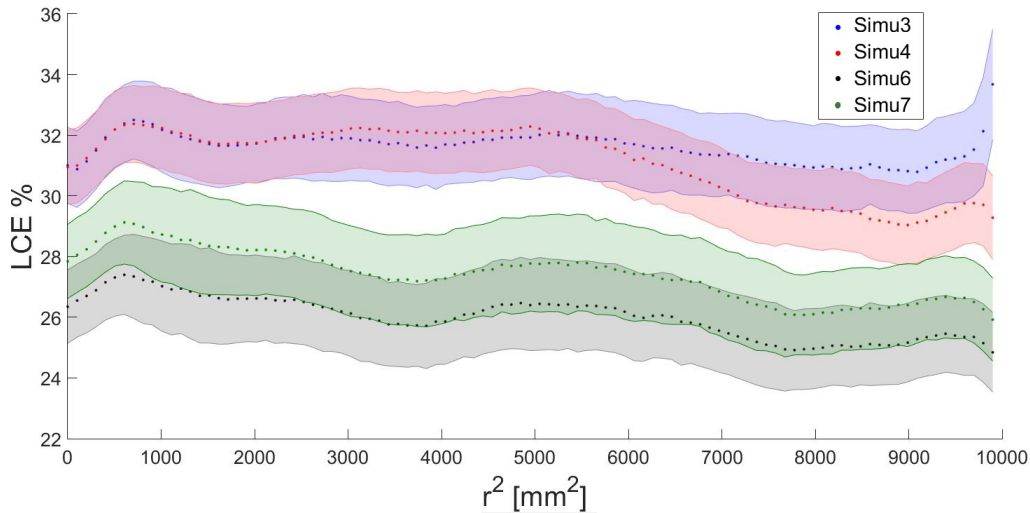


Figure 5.4: LCE for S2 for the top array as a function of r^2 . The shaded area represent the first standard deviation. Simulation 3 presents a better LCE than Simulation 4 in the outer region, this is due to the geometrical difference shown in figure 5.3. Simulation 7 presents a higher LCE in S2 respect to Simulation 6 given by the fact that in Simulation 7 the bottom reflective area is larger. Simulations 6 and 7 are described in section 5.1.8.

Using the data collected in Simulation 4, the homogeneity of the signal distribution for the different PD models has been analysed, and results are represented in figure 5.5. As expected the size of the detection area per model defines the individual average LCE. In Configuration 4 the 28 MPPCs with $12 \times 12 \text{ mm}^2$ area cover a bigger surface than the 12 APDs with an area of $14 \times 14 \text{ mm}^2$. The dominant contribution to the LCE is provided from the 21 1-inch PMTs. The smallest standard deviation, used to characterise the homogeneity, is reached by the APD with 1.1% and the highest by the 1-inch PMT with 1.7%. The total standard deviation for the light detected by the top array is 1.6%. The peaks are all well defined showing that not only the overall homogeneity is good, but also the one of the individual PD models, suggesting that the top PD array configuration has been chosen wisely.

5.1.8 Analysis of S1 Simulations

The simulation in S1 creates events everywhere in the LXe but only events produced above the cathode, situated 15 mm above the bottom PD holder, are considered. This is due to the fact that only the interactions between the cathode and gate grids are producing S1 and S2 signals, which are of interest for DM search (section 2.3.1). The initial design of the bottom PD array included five 3-inch PMT and one 1-inch PMT placed in the middle. Simulation 7 was performed using Simulation 6 configuration, without the central 1-inch PMT. This leads to a total LCE of $(61.3 \pm 1.6)\%$, compared to the $(61.9 \pm 1.5)\%$ obtained from Simulation 6. For this negligible

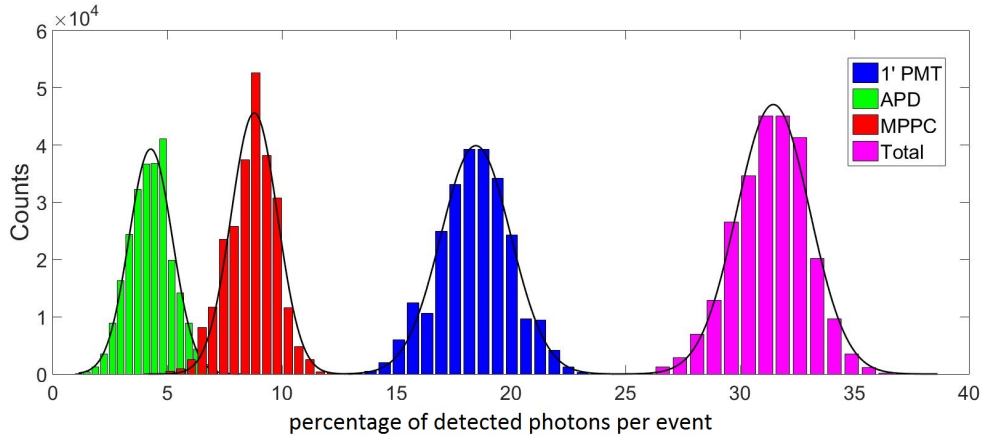


Figure 5.5: The histograms represent the number of events with a given percentage of photons detected by the top array during Simulation 4. The position of the peaks gives the LCE for the individual top array PD models and the total one. The width of the distributions provides information about the homogeneity.

difference, it has been decided that the effort of placing a 1-inch PMT was too high. The difficulties arise from its different geometry and operation voltage, compared to the 3-inch, a dedicated holder would be required. In figure 5.6 and 5.7 results obtained in S1 simulations are presented. The pattern of the bottom array can be seen by looking at the regions where the LCE is very high, corresponding to the events that are generated in front of a PD.

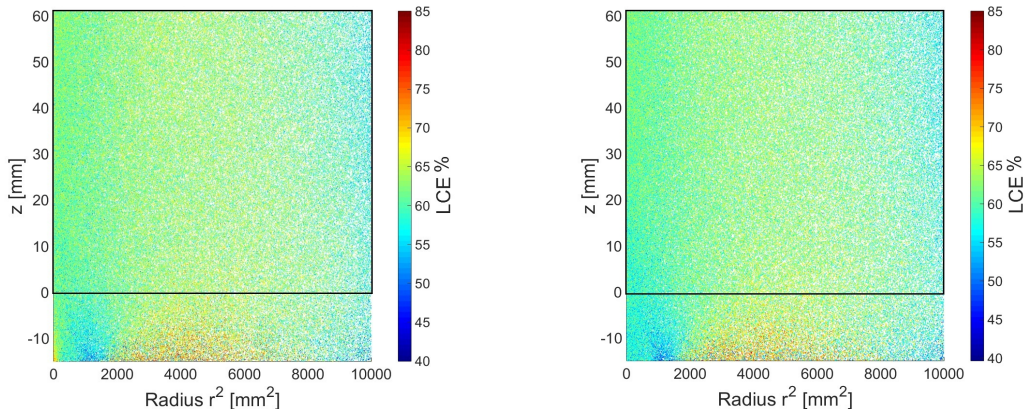


Figure 5.6: Comparison of the LCE for S1 for Simulation 6 and Simulation 7. In the bottom left corner ($r^2 < 1000 \text{ mm}^2$) the difference between the two simulations can be noticed, with a lower LCE on the right plot. Simulation 7 differs from Simulation 6 by the absence of the central 1-inch PMT, this has an impact of 1% on the LCE in the region of interest demarcated by the black frame.

The LCE in S1 is less affected by the changes in the top array since most of the photons are detected by the five 3-inch PMTs of the bottom array. Only minimal changes can be applied to improve the LCE by shaping the PD holes edges. Using the data collected in Simulation 7 the plots shown in figure 5.8 have been obtained, representing the LCE for the bottom and top arrays as well as both together. The smallness of the top array contributions can be easily seen comparing the colour bars.

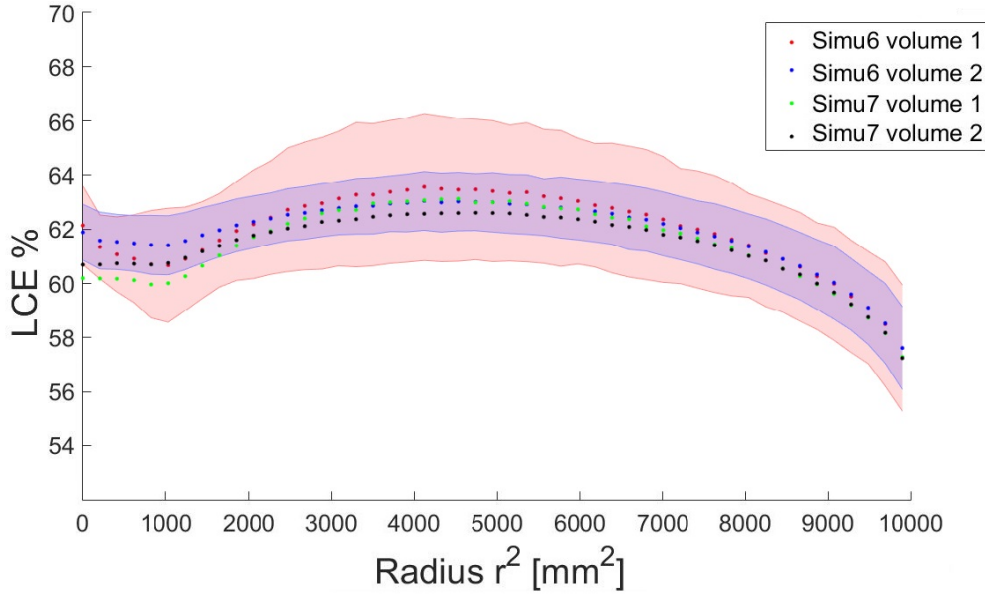


Figure 5.7: LCE in S1 as a function of r^2 for Simulation 6 and Simulation 7. Volume 1 and volume 2 are defined as the entire LXe volume, and the LXe volume above the cathode respectively. For both of these volumes the errors (shaded area corresponding to the standard deviation) have been represented for Simulation 6. Considering volume 2, the error becomes smaller and the overall standard deviation of the LCE is reduced by 1%. The difference in LCEs between the simulations 6 and 7 arises from the presence or absence of the central 1-inch PMT of the bottom array (see figure 5.6).

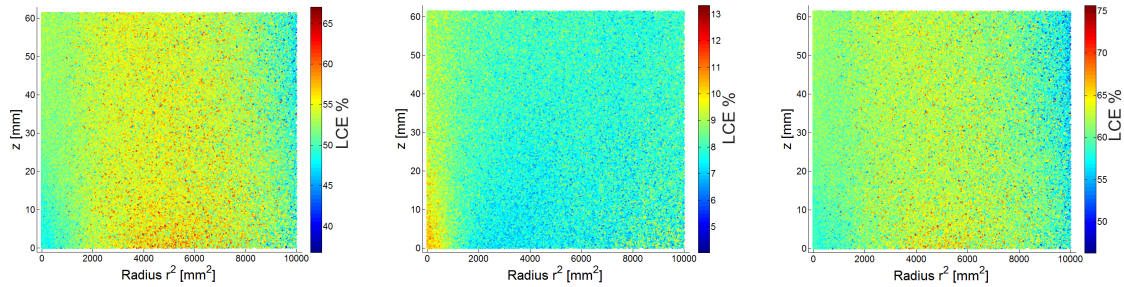


Figure 5.8: The LCE for S1 for events inside the area of interest for the bottom array (left), top array (middle), and both combined (right). The colour range is different in the three plots since the LCE range varies greatly between them.

5.2 Technical Drawing

5.2.1 Design of the Top Photodetector Array Holder

The technical drawing was performed using DS SolidWorks [82]. Through the tools available to the user it is possible to build every single part separately and then put them together in the final drawing. Models of the 1-inch PMT, the APDs and the MPPCs have also been realized as shown in figure 5.9.

In order to realise a suitable design of the top PTFE holder, such factors as the machine precision and material properties have to be considered:

- PTFE shrinks by 1.34% when cooled down from $+20^\circ\text{C}$ to -100°C [83]. Hence the PD could break under the PTFE pressure, since the thermal contraction coefficient of ceramic

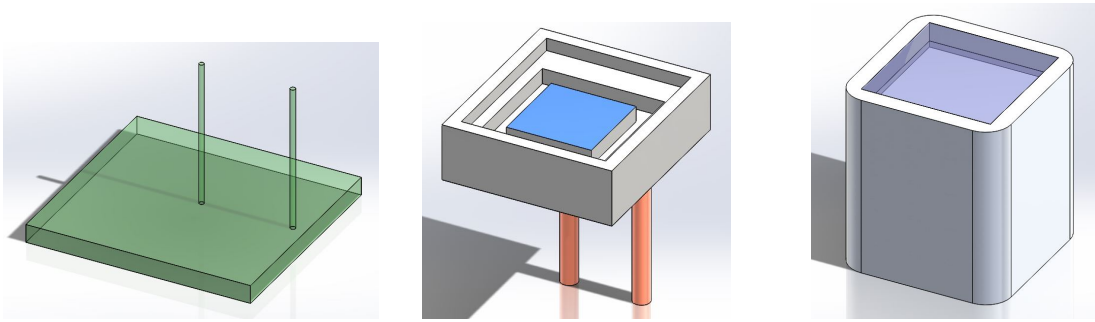


Figure 5.9: Technical drawings performed in DS SolidWorks: an APD (left), an MPPC (middle) and a PMT (right).

and quartz is two order of magnitude smaller. To prevent damage the hole for the PD was made 1.5% bigger than the PD.

- Drill bits used to build the support are circular, so inner corner can not be perfectly squared. The ratio between the drill bit radius and depth to be drilled is $1/6$. This has to be considered for all inner corners, and the adopted solution is shown in figure 5.10.

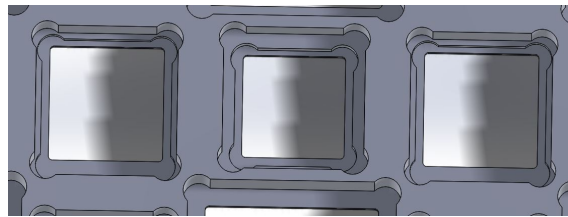


Figure 5.10: Design adopted to overcome the drill bits issue.

- Given their low mass MPPCs and APDs could move out of their position due to connection cable tension or turbulence produced during the filling procedure of the TPC. For this purpose a *fixer* has been designed taking into consideration the signal pins of APDs and MPPCs (see figure 5.11).

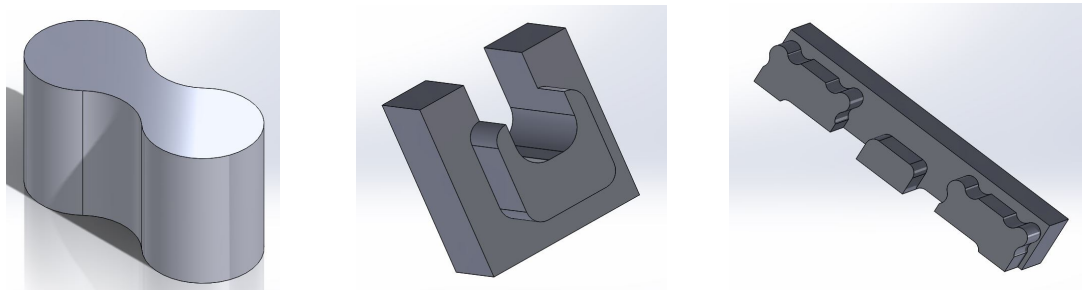


Figure 5.11: Three different PD *fixers*: the left and middle ones are designed to fix respectively a single APD and an MPPC. On the right a more complex drawing is given to keep in position two APDs, one $3 \times 3 \text{ mm}^2$ MPPC, as well as the PMT. The drawing on the right is a specific design for Configuration 1.

5.3 Conclusion to the TPC Project

Once the cylindrical design and the inner radius of the TPC have been fixed, Monte Carlo simulations with Geant4 have been performed. The main results of this study are:

- The optimal distance between the LXe surface and the top PD array has been obtained from the performed simulations and is equivalent to 2.25 cm. This result is in agreement with the one obtained for the XENON100 simulation, where the optimal distance is similar to the size of the 1-inch PMTs used. Combining the 1-inch PMTs with smaller PDs such as MPPCs and APDs reduces this distance.
- The design including only five 3-inch PMTs for the bottom array is preferred to the one with an additional 1-inch PMT, as the effort required to place and operate it does not justify the sub-percent improvement in LCE.
- Giving a slope to the holes of the PMT increases a slightly the LCE, but if a larger number of PDs is available the space can be used for them instead.
- $3 \times 3 \text{ mm}^2$ MPPCs present a too small detection area and should not be used for this TPC. Even in simulation with eight devices the LCE was less than 1%. To make this kind of PD useful, a model with a larger active area and a large number has to be used. As shown in figure 5.5, 28 MPPCs with an $12 \times 12 \text{ mm}^2$ area provide a LCE in S2 of 8.8%. The disadvantage of using a lot of MPPCs is the amount of readout channels. On the other hand, the advantage is that they provide precise position information that improves the resolution of the reconstructed interaction point.

All the obtained LCEs presented so far do not take into account the quantum efficiency (QE) of the different detectors (see section 3.2). For the geometry optimisation of the TPC a $\text{QE} = 100\%$ has been assumed. The data collected have been used for the determination of the best geometry, and are not directly comparable with the result that could be obtained from the real experiment. In order to give an idea of a more realistic lower-limit on the LCE of the TPC, the quantum efficiency of the specific PD models has been applied to the results of Simulation 7 (PDs QE [84]). The amount of light collected by different types of sensors as well as the standard deviations have been obtained with the same method as shown in figure 5.5. For the simulation in S1 only the events generated above the cathode are considered. These results, together with the QE of the different PD models, and the resulting light collection efficiency LCE_{RES} for S1 and S2 are presented in the tables 5.4 and 5.5. It can be seen that 53.1% and 40.0% of the light produced in S1 respectively S2 is collected by the five 3-inch PMTs of the bottom array. They represent 63% of the total detection area of the TPC.

Simulation 7 takes into account all the information collected from the previous simulations. This corresponds to the optimal configuration for 21 1-inch PMTs, 12 APDs, and 8 MPPCs ($12 \times 12 \text{ mm}^2$) for the top array, and 5 3-inch PMTs for the bottom array. The technical drawing of the top array holder with this photosensor pattern is shown in figure 5.12.

Assuming $\times 10$ longer absorption length and PTFE reflectivity of 99%, as in the recent publication from XENON1T [56], an increase in the total LCE of $\sim 10\%$ is expected for MarmotXL TPC.

Table 5.4: LCE for S1 for the different photosensor models in Simulation 7 considering their QE

	no. detectors	LCE [%]	QE [%]	LCE_{RES} [%]
APD	12	1.6 ± 0.3	28	0.4 ± 0.1
1-inch PMT	21	5.8 ± 0.6	30	1.8 ± 0.2
3-inch PMT	5	53.1 ± 1.9	33	17.0 ± 0.7
MPPC $12 \times 12 \text{ mm}^2$	8	0.8 ± 0.3	28	0.3 ± 0.1
Total	46	61.3 ± 1.5		19.5 ± 0.7

Table 5.5: LCE for S2 for the different photosensor models in Simulation 7 considering their QE

	no. detectors	LCE [%]	QE [%]	LCE_{RES} [%]
APD	12	4.3 ± 0.9	28	1.2 ± 0.3
1-inch PMT	21	20.9 ± 1.9	30	6.3 ± 0.6
3-inch PMT	5	40.0 ± 1.4	33	13.2 ± 0.9
MPPC $12 \times 12 \text{ mm}^2$	8	2.5 ± 1.4	28	0.7 ± 0.4
Total	46	68.0 ± 1.3		21.4 ± 0.8

Figure 5.12: SolidWorks drawing of the top array holder for twenty-one 1-inch PMT, twelve ADP and eight $12 \times 12 \text{ mm}^2$ MPPC.

Chapter 6

Summary

A design study for a time-projection chamber with hybrid photosensor arrays has been performed. The goal was to optimise the TPC geometry in order to obtain the highest possible particle detection efficiency, which is correlated with the light collection efficiency and its homogeneity. The TPC geometry studies have been performed with Monte Carlo simulations using Geant4. It has been noted that the LCE is strongly correlated with the reflectivity of the PTFE components and the absorption length of the LXe to scintillation light. The results presented in this thesis have been obtained setting the PTFE reflectivity to 95 % and the absorption length of LXe to 5 m. Variation of 4 % in reflectivity can cause LCE changes up to 10 %. For the optimised geometry of a TPC with 21 1-inch PMTs, 12 APDs, and 8 MPPCs ($12 \times 12 \text{ mm}^2$) for the top array, and 5 3-inch PMTs for the bottom array, the QEs of the different PD models have been taken into account. The overall LCE for S1 resulted to be 19.4 % and slightly higher for S2 with 21.4 %. Relevant is also the 8.2 % LCE in S2 of the top array, which provides the information for the x-y position reconstruction.

The requirement of extremely low background for the next generations of TPCs used for the study of dark matter, solar neutrinos and neutrinoless double beta decay, has lead to consider APD and MPPC as possible for such experiments. The use of these photosensors is supported by their low associated radiation and high detection surface-to-mass ratio. Tests performed at room temperature for three different MPPC models ($3 \times 3 \text{ mm}^2$) are presented in chapter 4. These devices have been demonstrated to provide sharp signals, enabling to distinguish up to the quadruple photoelectron events with the resolution on SPE of $\sim 15\%$. A stable power supply (mV) has to be used, since an increase of the operation voltage of 10 mV makes the gain rise by 5 %. In order to obtain a clear single photon spectrum a $\times 10$ amplifier had to be used. Furthermore, the pick-up of electronic noise has to be kept low, this has been achieved by using double shielded cables for the entire electronic set-up.

Concerning the 1-inch PMTs, their amplification factors have been characterized at room temperature using a dedicated set-up. The dependency of the gain on the operation voltage has been studied for 23 PMTs (model R8520-406). One has been found to be not working. The same PMT model has been tested and installed in XENON100. The results obtained match in gain and resolution the previous tested PMTs.

The tests performed with the MPPCs have provided the knowledge required to operate these photosensors at room temperature, and their temperature dependency has been studied. Next, the $3 \times 3 \text{ mm}^2$ MPPCs will be tested in LXe, and a new MPPC with an area of $12 \times 12 \text{ mm}^2$, four $6 \times 6 \text{ mm}^2$ MPPCs joined together, will be tested. The first task is the realisation of a base allowing to read out the four channels simultaneously.

This work provides the first steps for the realisation of a TPC with a hybrid photosensor array. It will be used to study the position and energy reconstruction at energies above $\sim 1 \text{ MeV}$ relevant

for double-beta decay searches with ^{136}Xe , required for the design of the DARWIN experiment.

Chapter 7

Acknowledgement

Working on this project made me face problems arising from my lack of experience. Some of them could be overcome in a natural process by trial and error. Others required the support of more experienced persons, who helped me to close my knowledge gaps.

I would like to express my gratitude to Dr. Prof. Laura Baudis who gave me the opportunity to work on this challenging project as part of her group. A special thanks goes to Alexander Kish that supervised me editing my thesis.

During my daily work I could rely on Payam Pakarha, Giovanni Benato and Francesco Piastra for problem concerning the software and Julien Wulf and Gaudenz Kessler for the hardware. To mention is also the contribution I got from all the members of the group during the weekly meetings. To conclude, a great thanks goes to Roman Gredig, who shared his knowledge on MPPCs with me and lent to me one of his MPPC base. This enabled me to obtain the first single photon spectrum and therefore to identify the operation voltage of our MPPCs.

Bibliography

- [1] Kevin Joseph Lung. *The search for dark matter in XENON100 using a two-dimensional profile Likelihood analysis*. PhD thesis, University of California-Los Angeles (UCLA), 2013, http://home.physics.ucla.edu/~arisaka/Thesis/Kevin_Lung_Thesis.pdf.
- [2] P. Peebles and B. Ratra. *The Cosmological constant and dark energy*. Rev.Mod.Phys., vol. 75, 2003.
- [3] D. Spergel et al. *Wilkinson Microwave Anisotropy Probe (WMAP) three year results: implications for cosmology*. Astrophys.J.Suppl., vol. 170, p. 377, 2003.
- [4] The Planck Collaboration. *Planck 2015 results. XIII. Cosmological parameters*. arXiv:1502.01589.
- [5] V. Lukovic, P. Cabella, and N. Vittorio. *Dark matter in cosmology*. International Journal of Modern Physics A, 2014.
- [6] V. C. Rubin, N. Thonnard, and J. Ford. *Extended rotation curves of high-luminosity spiral galaxies*. Astrophys. J 225 L107, 1978.
- [7] T. S. Van Albada, R. Sancisi, Maria Petrou, and R. J. Tayler. *Dark Matter in Spiral Galaxies [and Discussion]*. Philosophical Transactions of the Royal Society of London, 1986.
- [8] K. Begeman, A. Broeils, and R. Sanders. *Extended rotation curves of spiral galaxies: Dark haloes and modified dynamics*. Mon.Not.Roy.Astron.Soc., vol. 249, 1991.
- [9] Ciaran A. J. O'Hare and Anne M. Green. *Directional detection of dark matter streams*. Phys. Rev. D 90, 123511, 2014.
- [10] Ramesh Narayan and Matthias Bartelmann. *Lectures on Gravitational Lensing*. arXiv:astro-ph/9606001, 2014.
- [11] Emma Grocutt. *What is Gravitational Lensing?* CFHTLenS, 2015, <http://www.cfhtlens.org/public/what-gravitational-lensing>.
- [12] Massimo Meneghetti. *Introduction to Gravitational Lensing*. Lecture script Uni Heidelberg, http://www.ita.uni-heidelberg.de/~massimo/sub/Lectures/gl_all.pdf.
- [13] Stefano Scopel. *Particle Dark Matter Candidates*. J.Phys.Conf.Ser.120:042003, 2008.
- [14] John F. Beacom Gary Steigman, Basudeb Dasgupta. *Precise Relic WIMP Abundance and its Impact on Searches for Dark Matter Annihilation*. Phys.Rev. D86 023506, 2012.
- [15] G. Steigman and M. S. Turner. Nucl, Phys. B253, 375-386, 1985.
- [16] Bobby Samir Acharya, Piyush Kumar, Gordon Kane, and Scott Watson. *A Non-thermal WIMP Miracle*. Phys.Rev.D80:083529, 2009.
- [17] J. L. Feng. *Dark matter candidates from particle physics and methods of detection*. Annual Review of Astronomy and Astrophysics Vol. 48: 495-545, 2010.

- [18] R. Peccei and H. R. Quinn. *CP Conservation in the Presence of Instantons*. Phys.Rev.Lett., vol. 38, pp. 1440-1443, 1977.
- [19] P. Sikivie. *Superconducting Radio Frequency Cavities as Axion Dark Matter Detectors*. arXiv:1009.0762, 2010.
- [20] Max Planck Gesellschaft. *Research: Dark Matter*. Max-Planck-Institut für Kernphysik, 2015.
- [21] Marco Cirell, Gennaro Corcella, Andi Hektor, Mario Kadastik, Paolo Panci, Martti Raidal, Filippo Sala, and Alessandro Strumia. *PPPC 4 DM ID: A Poor Particle Physicist Cookbook for Dark Matter Indirect Detection*. JCAP 1103:051, 2011.
- [22] CERN Accelerating science. *The large Hadron Collider*. <http://home.web.cern.ch/topics/large-hadron-collider>.
- [23] Steven Lowette. *Search for dark matter at CMS*. arXiv:1410.3762v2, 2014.
- [24] G. Jungman, M. Kamionkowski, , and K. Griest. *Supersymmetric dark matter*. Phys.Rept., vol. 267, pp. 195-373, 1996.
- [25] J. Lewin and P. Smith. *Review of mathematics, numerical factors, and corrections for dark matter experiments based on elastic nuclear recoil*. Astropart.Phys., vol. 6, pp. 87-112, 1996.
- [26] The University of Sheffield. *Dark Matter Research, 2015*,. <https://www.hep.shef.ac.uk/research/dm/intro.php>.
- [27] Andrzej K. Drukier, Katherine Freese, and David N. Spergel. *Detecting cold dark-matter candidates*. Phys. Rev. D 33, 3495.
- [28] Katherine Freese, Joshua Frieman, and Andrew Gould. *Signal modulation in cold-dark-matter detection*. Phys. Rev. D 37, 3388, 1988.
- [29] D. N. Spergel. *The Motion of the Earth and the Detection of Weakly interacting massive particles*. Phys. Rev. D37 1353., 1988.
- [30] R. Bernabei, P. Belli, and A. Di Marco. *DAMA/LIBRA results and perspectives*. 15th Bled Workshop “What Comes Beyond Standard Models”, Vol. 13, No. 2, 2012.
- [31] E. Aprile et al. (The XENON100 Collaboration). *The XENON100 Dark Matter Experiment*. Astropart. Phys. 35/9, 573-590, 2012.
- [32] D. S. Akerib et al. (The LUX Collaboration). *The Large Underground Xenon (LUX) Experiment*. Nuclear Inst. and Methods in Physics Research A704, pages 111-126, 2013.
- [33] J. Cooley. *Overview of Non-Liquid Noble Direct Detection Dark Matter Experiments*. Phys. Dark Univ. volume 4, pages 92-97, 2014.
- [34] Cristina Maria and Bernardes Monteiro. *Determination of argon and xenon absolute electroluminescence yields in Gas Proportional Scintillation Counters*. University of Coimbra, 2010.
- [35] J. et al. Kwong. *Scintillation Pulse Shape Discrimination in a Two-Phase Xenon Time Projection Chamber*. Nucl.Instrum.Meth. A612 328-333, 2010.
- [36] M. Moongweluwan. *The Impact of Photon Flight Path on S1 Pulse Shape Analysis in Liquid Xenon Two-phase Detectors*. Journal of Instrumentation, Volume 11, 2016.
- [37] E. Aprile, R. Mukherjee, and M. Suzuki. *Performance of a liquid xenon ionization chamber irradiated with electrons and gamma-rays*. Nucl.Instrum.Meth., vol. A302, pp. 177-185, 1991.
- [38] *Dark Matter*. UCL, 2015, <http://www.hep.ucl.ac.uk/darkMatter/>.

- [39] M. Szydagis, N. Barry, K. Kazkaz, and J. Mock. *NEST: A Comprehensive Model for Scintillation Yield in Liquid Xenon*. arXiv:1106.1613, 2012.
- [40] A. Manzur et al. *Scintillation efficiency and ionization yield of liquid xenon for mono-energetic nuclear recoils down to 4 keV*. Phys. Rev. C 81, 025808, 2010.
- [41] G. Plante et al. *New Measurement of the Scintillation Efficiency of Low-Energy Nuclear Recoils in Liquid Xenon*. Phys. Rev. C 84, 045805, 2011.
- [42] V. Alvarez et al. (The NEXT Collaboration). *Ionization and scintillation response of high-pressure xenon gas to alpha particles*. JINST, 2013.
- [43] Y-F. Wang, V. Balic, and G. Gratta. *Predicting neutron production from cosmic-ray muons*. Phys. Rev. D, Volume 64, 2001.
- [44] D.-M. Mei and A. Hime. *Muon-Induced Background Study for Underground Laboratories*. Phys.Rev.D73:053004, 2006.
- [45] E. Aprile et al. (The XENON100 Collaboration). *The neutron background of the XENON100 dark matter search experiment*. arXiv:1306.2303v2, 2013.
- [46] Louis E. Strigari. *Neutrino Coherent Scattering Rates at Direct Dark Matter Detectors*. New J.Phys.11:105011, 2009.
- [47] F. Ruppin, J. Billard, E. Figueroa-Feliciano, and L. Strigari. *Complementarity of dark matter detectors in light of the neutrino background*. Phys. Rev. D 90, 083510, 2014.
- [48] D.S. Akerib et al. (The LUX Collaboration). *Radiogenic and Muon-Induced Backgrounds in the LUX Dark Matter Detector*. Astropart.Phys. 62 33-46, 2015.
- [49] Laura Baudisa, Alexander Kishb, Francesco Piastrac, and Marc Schumannnd. *Cosmogenic activation of xenon and copper*. arXiv:1507.03792, 2015.
- [50] E. Aprile et al. (The XENON100 Collaboration). *Material screening and selection for XENON100*. Astropart.Phys.35:43-49, 2011.
- [51] E. Aprile et al. (The XENON Collaboration). *Lowering the radioactivity of the photomultiplier tubes for the XENON1T dark matter experiment*. arXiv:1503.07698, 2015.
- [52] J. Angle et al. (The XENON10 Collaboration). *First Results from the XENON10 Dark Matter Experiment at the Gran Sasso National Laboratory*. Phys.Rev.Lett.100:021303, 2008.
- [53] E. Aprile et al. (The XENON Collaboration). *Dark Matter Results from 225 Live Days of XENON100 Data*. Phys. Rev. Lett. 109, 181301, 2012.
- [54] E. Aprile et al. (The XENON Collaboration). *The XENON1T Dark Matter Search Experiment*. arXiv:1206.6288v1, 2012.
- [55] E. Aprile, F. Agostini, M. Alfonsi, K. Arisaka, F. Arneodo, M. Auger, C. Balan, P. Barrow, and L. Baudis. *Conceptual design and simulation of a water Cherenkov muon veto for the XENON1T experiment*. JINST 9, P11006, 2014.
- [56] E. Aprile et al. (The XENON Collaboration). *Physics reach of the XENON1T dark matter experiment*. arXiv:1512.07501, 2015.
- [57] L. Baudis, A. Ferella, A. Kish, A. Manalaysay, T. Marrodan Undagoitia, and M. Schumann. *Neutrino physics with multi-ton scale liquid xenon detectors*. JCAP01 044, 2014.
- [58] Marc Schumann for the DARWIN Consortium. *DARWIN*. arXiv:1111.6251, 2011.
- [59] M. Auger et al. (The EXO Collaboration). *Search for Neutrinoless Double-Beta Decay in Xe-136 with EXO-200*. Phys. Rev. Lett. 109 032505, 2012.

- [60] A. Gando et al. (The KamLAND-Zen Collaboration). *Limit on Neutrinoless Double Beta Decay of Xe-136 from the First Phase of KamLAND-Zen and Comparison with the Positive Claim in Ge-76*. Phys. Rev. Lett. 110 6, 062502, 2013.
- [61] I. Ostrovskiy et al. *Characterization of silicon photomultipliers for nEXO*. Nuclear Science, IEEE Transactions on , vol.62, no.4, pp.1825,1836, 2015.
- [62] Marc Schumann, Laura Baudis, Lukas Buetikofer, Alexander Kish, and Marco Selvi. *Dark matter sensitivity of multi-ton liquid xenon detectors*. JCAP 10, 016, 2015.
- [63] Andrea Gmuer. *Photomultiplier Tube Tests in Liquid Xenon for Direct Dark Matter Detection Experiments*. Bachelor thesis, University of Zurich, 2013, http://www.physik.uzh.ch/groups/groupbaudis/darkmatter/theses/xenon/bachelor_gmuer.pdf.
- [64] Michael Miloradovic. *Avalanche Photodiode (APD) Testing in Liquid Xenon*. Bachelor thesis, University of Zurich, 2013, www.physik.uzh.ch/groups/groupbaudis/darkmatter/theses/xenon/bachelor_miloradovic.pdf.
- [65] Hamamatsu. *Photomultiplier tube, Basics and Applications*. Third Edition. Hamamatsu Photonics K.K., Electron Tube Division, 2006.
- [66] Cirlex. <http://www.cirlex.com/>.
- [67] Hamamatsu. *Photomultiplier Tube R8520-406, 2015*. http://www.hamamatsu.com/resources/pdf/etd/R8520-406_TPMH1342E.pdf.
- [68] Sandro D'Amato. *SandBox: A facility for XENON photosensors characterization and measurements of photocathode uniformity*. Bachelor thesis, University of Zurich, 2014, http://www.physik.uzh.ch/groups/groupbaudis/darkmatter/theses/xenon/bachelor_damato.pdf.
- [69] Alexander Kish. *Dark Matter Search with the XENON100 Experiment*. PhD thesis, University of Zurich, 2011, <http://opac.nebis.ch/ediss/20121322.pdf>.
- [70] Hamamatsu. *Hamamatsu Opto-Semiconductor Handbook, 2014*. https://www.hamamatsu-news.de/hamamatsu_optosemiconductor_handbook/.
- [71] Modern Lab Experiments documentation. *PN-Junction*. http://wanda.fiu.edu/teaching/courses/Modern_lab_manual/pn_junction.html.
- [72] Electronics-tutorials. http://www.electronics-tutorials.ws/diode/diode_4.html.
- [73] A. Stoykov and R. Scheuerman. *Silicon Avalanche Photodiodes*. Laboratory for Muon Spin Spectroscopy, 2004.
- [74] Manuel Walter. *Background Reduction Techniques for the Gerda Experiment*. PhD thesis at the University of Zurich, 2015, http://www.zora.uzh.ch/113939/1/thesis_ManuelWalter_PhD.pdf.
- [75] Niklaus Berger et al. (The Mu3e Collaboration). *The Mu3e Experiment*. Nuclear Physics B Proceedings Supplement 00 1-6, 2013.
- [76] Benjamin K. Tsai, David W. Allen, and Leonard M. Hanssen. *A Comparison of Optical Properties between High Density and Low Density Sintered PTFE*. National Institute of Standards and Technology, 2008.
- [77] Min K. Yang and Roger H. French. *Optical properties of Teflon AF amorphous fluoropolymers*. Journal of Micro/Nanolithography, MEMS and MOEMS 7(3), 033010, 2008.
- [78] *Optical PTFE: The reference for light*. Berghof, <http://www.berghof.com/fileadmin/Dateien-Einpflege/Seitenbaum/Home-Downloads/Produkte/PTFE-Produkte/Optisches>

- [79] M. Yamashita et al. *Scintillation response of liquid Xe surrounded by PTFE reflector for gamma rays*. Nucl. Instrum. Methods Phys. Res. Sect. A 535, 692-698, 2004.
- [80] C. Silva, J. Pinto da Cunha, A. Pereira, V. Chepel, M. I. Lopes, and V. Solovov. *Reflectance of Polytetrafluoroethylene (PTFE) for Xenon Scintillation Light*. arXiv:0910.1056, 2009.
- [81] Maria Grazia Pia. *The Geant4 Object Oriented Simulation Toolkit*. CERN; IT Division, 1995.
- [82] SolidWorks homepage. <http://www.solidworks.com>.
- [83] *Properties Handbook: Teflon PTFE fluoropolymer resin*. DuPont, 2015.
- [84] Hamamatsu. *Data sheet of the photodetectors (not public document)*.



Eidgenössische Technische Hochschule Zürich
Swiss Federal Institute of Technology Zurich

Institute for Dynamic Systems and Control
Prof. Dr. R. D'Andrea, Prof. Dr. L. Guzzella

Title of work:

Design of a Dual-phase Xenon Time-projection Chamber with
a Hybrid Photosensor Arrays

Thesis type and date:

Master Thesis, 2016

Supervision:

Prof. Dr. Laura Baudis
Dr. Alexander Kish

Student:

Name: Andrea Gmür
E-mail: gmueran@access.uzh.ch
Legi-Nr.: 08-918-500
Semester: 8-10

Statement regarding plagiarism:

By signing this statement, I affirm that I have read and signed the Declaration of Originality, independently produced this paper, and adhered to the general practice of source citation in this subject-area.

Declaration of Originality:

http://www.ethz.ch/faculty/exams/plagiarism/confirmation_en.pdf

Zurich, 15. 7. 2016: _____